

THE DEACTIVATION STUDY OF TITANIUM DIOXIDE CATALYST IN THERMOCHEMICAL  
PROCESSES VIA DENSITY FUNCTIONAL THEORY



A Thesis Submitted in Partial Fulfillment of the Requirements  
for the Degree of Master of Engineering in Chemical Engineering

Department of Chemical Engineering

FACULTY OF ENGINEERING

Chulalongkorn University

Academic Year 2020

Copyright of Chulalongkorn University

การศึกษาความเสื่อมสภาพของตัวเร่งปฏิกิริยาไทเทเนียมไดออกไซด์ในกระบวนการทางเคมีความร้อน  
โดยทฤษฎีฟังก์ชันนอลความหนาแน่น



วิทยานิพนธ์นี้เป็นส่วนหนึ่งของการศึกษาตามหลักสูตรปริญญาวิศวกรรมศาสตรมหาบัณฑิต  
สาขาวิชาวิศวกรรมเคมี ภาควิชาวิศวกรรมเคมี  
คณะวิศวกรรมศาสตร์ จุฬาลงกรณ์มหาวิทยาลัย  
ปีการศึกษา 2563  
ลิขสิทธิ์ของจุฬาลงกรณ์มหาวิทยาลัย

Thesis Title	THE DEACTIVATION STUDY OF TITANIUM DIOXIDE CATALYST IN THERMOCHEMICAL PROCESSES VIA DENSITY FUNCTIONAL THEORY
By	Miss Chinanang Ngamlaor
Field of Study	Chemical Engineering
Thesis Advisor	Assistant Professor SUPAREAK PRASERTHDAM, Ph.D.
Thesis Co Advisor	Tinnakorn Saelee, Ph.D.

---

Accepted by the FACULTY OF ENGINEERING, Chulalongkorn University in  
Partial Fulfillment of the Requirement for the Master of Engineering

..... Dean of the FACULTY OF  
ENGINEERING  
(Professor SUPOT TEACHAVORASINSKUN, D.Eng.)

#### THESIS COMMITTEE

..... Chairman  
(Professor TAWATCHAI CHARINPANITKUL, D.Eng.)

..... Thesis Advisor  
(Assistant Professor SUPAREAK PRASERTHDAM, Ph.D.)

..... Thesis Co-Advisor  
(Tinnakorn Saelee, Ph.D.)

..... Examiner  
(Professor BUNJERD JONGSOMJIT, Ph.D.)

..... Examiner  
(Professor VITHAYA RUANGPORNVISUTI, Ph.D.)

..... External Examiner  
(Pussana Hirunsit, Ph.D.)

ชื่อนาง งามละอ : การศึกษาความสัมพันธ์ของตัวเร่งปฏิกิริยาไทเทเนียมไดออกไซด์ในกระบวนการทางเคมีความร้อนโดยทฤษฎีฟังก์ชันนอลความหนาแน่น . ( THE DEACTIVATION STUDY OF TITANIUM DIOXIDE CATALYST IN THERMOCHEMICAL PROCESSES VIA DENSITY FUNCTIONAL THEORY) อ.ที่ปรึกษาหลัก : ผศ. ดร.ศุภฤกษ์ ประเสริฐธรรม, อ.ที่ปรึกษาร่วม : ดร.ทินกร แซ่หลี่

ในการศึกษานี้ได้ทำการศึกษาการเสื่อมสภาพของตัวเร่งปฏิกิริยาไทเทเนียมไดออกไซด์โดยใช้ทฤษฎีฟังก์ชันนอลความหนาแน่น โดยศึกษาผลของการเพิ่มคุณสมบัติทางอิเล็กทรอนิกส์จากเทอมของฮับบาร์ดในช่วง 4-6 อิเล็กตรอนโวลต์ที่มีการเกี่ยวกับแรงวานเดอร์วาลส์รวมถึงผลของอุณหภูมิช่วง 400-1000 องศาเซลเซียส เพื่อศึกษาความสัมพันธ์ระหว่างการก่อตัวของโค้ก การเกิดออกซิเจนวาแคนซีและการเปลี่ยนเฟส จากผลการทดลองพบว่ากรณีที่เทอมของฮับบาร์ดมีค่าเพิ่มขึ้นนั้นสามารถทำให้มีความแม่นยำมากขึ้น ซึ่งค่าของเทอมฮับบาร์ดที่เหมาะสมของเฟสอะนาเทสคือ 4 อิเล็กตรอนโวลต์ ในขณะที่ในเฟสของรูไทล์คือ 6 อิเล็กตรอนโวลต์ ซึ่งการก่อตัวของโค้กของสำหรับพื้นผิวที่สมบูรณ์นั้นคาร์บอน 1 อะตอม จะถูกดูดซับอย่างมากบนพื้นผิวเฟสอะนาเทสในขณะที่การก่อตัวของคาร์บอน 2 อะตอมถูกดูดซับอย่างมากบนพื้นผิวของเฟสรูไทล์ จากผลของการเกิดออกซิเจนวาแคนซีในการก่อตัวของโค้กพบว่าคาร์บอน 2 อะตอมถูกดูดซับอย่างมากบนพื้นผิวของทั้งเฟสอะนาเทสและรูไทล์ ซึ่งเป็นไปได้ว่าพื้นผิวที่มีการเกิดออกซิเจนวาแคนซีนั้นมีความว่องไวต่อปฏิกิริยามากกว่าพื้นผิวที่สมบูรณ์ซึ่งอาจนำไปสู่ความเสถียรที่สูงขึ้นของการสะสมของโค้ก สำหรับผลของอุณหภูมินั้นเมื่ออุณหภูมิเพิ่มขึ้นพบว่าปฏิสัมพันธ์ระหว่างโค้กและพื้นผิวตัวเร่งปฏิกิริยาจะอ่อนแอลง นอกจากนี้ในกระบวนการทางเคมีความร้อนตัวเร่งปฏิกิริยาไทเทเนียมไดออกไซด์สามารถเปลี่ยนเฟสจากอะนาเทสเป็นรูไทล์ได้ ซึ่งเป็นไปได้ว่าการก่อตัวของโค้กบนพื้นผิวของรูไทล์มีความเสถียรมากกว่าบนพื้นผิวของอะนาเทส

สาขาวิชา วิศวกรรมเคมี

ปีการศึกษา 2563

ลายมือชื่อนิสิต .....

ลายมือชื่อ อ.ที่ปรึกษาหลัก .....

ลายมือชื่อ อ.ที่ปรึกษาร่วม .....

# # 6270065721 : MAJOR CHEMICAL ENGINEERING

KEYWORD: Titanium dioxide, coke formation, Density Functional Theory (DFT),  
The Hubbard U, D3 dispersion

Chinanang Ngamlaor : THE DEACTIVATION STUDY OF TITANIUM DIOXIDE CATALYST IN THERMOCHEMICAL PROCESSES VIA DENSITY FUNCTIONAL THEORY. Advisor: Asst. Prof. SUPAREAK PRASERTHDAM, Ph.D. Co-advisor: Tinnakorn Saelee, Ph.D.

In this study, the investigation of catalytic deactivation of  $\text{TiO}_2$  by coking was performed using DFT. The effect of the Hubbard U, which was varied as U equal 4 to 6 eV and Van der Waal corrections on electronic properties were also investigated. The effect of temperature in the range of 400-1000°C was also studied. This work aims to understand relatives of coke formation, oxygen vacancy, phase transformation. The increment of the Hubbard U values provide a more accurate quantitative cited by the energy gap from the experimental investigation, the appropriate U value of the A- $\text{TiO}_2$  (101) is 4 eV, while the R- $\text{TiO}_2$  (110) is 6 eV. The coke formation of C1 is strongly adsorbed on the A- $\text{TiO}_2$  (101) surface, while on the R- $\text{TiO}_2$  (110) surface, C2 is strongly adsorbed. For oxygen vacancy on coke formation, C2 coke is strongly adsorbed on O-vac A- $\text{TiO}_2$  (101) and O-vac R- $\text{TiO}_2$  (110) surfaces. This can be suggested that the defect surface is more active than the perfect surface which may lead to higher stability of coke deposition. For the effect of temperature, the interaction between cokes and surfaces becomes weaker when the temperature is increased. Moreover, during the thermochemical process, the  $\text{TiO}_2$  catalyst can transform anatase to the rutile phase. It is suggested that the coke formation on the R- $\text{TiO}_2$  (110) surface is more severe than on the A- $\text{TiO}_2$  (101) surface.

Field of Study: Chemical Engineering

Academic Year: 2020

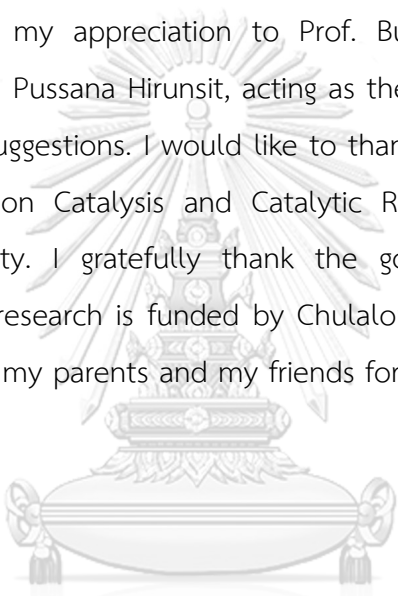
Student's Signature .....

Advisor's Signature .....

Co-advisor's Signature .....

## ACKNOWLEDGEMENTS

I would like to express my sincere thanks to my thesis advisor, Asst. Prof. Supareak Prasertthdam and my co-advisor, Dr. Tinnakorn Saelee to give me advice, guidance, suggestions and support during experimentation and discussion to achieve my thesis. I am extremely appreciative of their guidance and instruction, not only the research methodologies but also many other methodologies in life. In addition, I am also grateful to Prof. Tawatchai Charinpanitkul represented as the leader. Furthermore, I would like to extend my appreciation to Prof. Bunjerd Jongsomjit, Prof. Vithaya Ruangpornvisuti and Dr. Pussana Hirunsit, acting as the thesis committee, for providing additional welcomed suggestions. I would like to thank members and scientists in the Center of Excellence on Catalysis and Catalytic Reaction, Faculty of Engineering, Chulalongkorn University. I gratefully thank the government budget for financial support from CE. This research is funded by Chulalongkorn University. Finally, I most gratefully acknowledge my parents and my friends for all their support throughout the period of this research.



จุฬาลงกรณ์มหาวิทยาลัย  
CHULALONGKORN UNIVERSITY

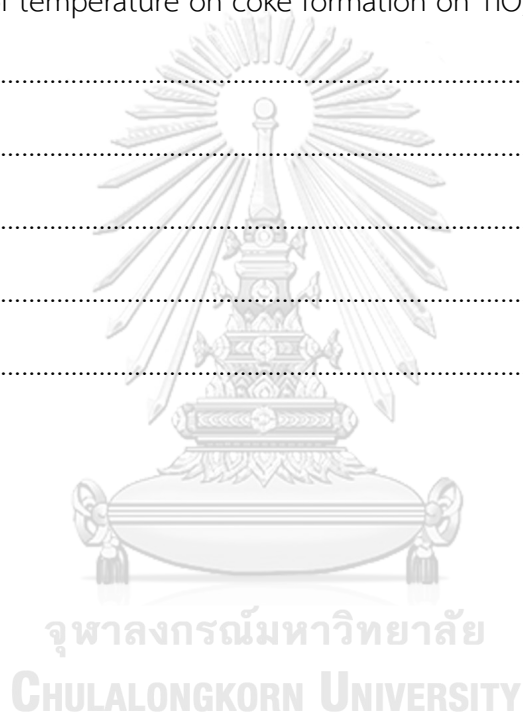
Chinanang Ngamlaor

## TABLE OF CONTENTS

	Page
.....	iii
ABSTRACT (THAI).....	iii
.....	iv
ABSTRACT (ENGLISH).....	iv
ACKNOWLEDGEMENTS .....	v
TABLE OF CONTENTS.....	vi
LIST OF TABLES.....	ix
LIST OF FIGURES .....	x
CHAPTER I.....	1
INTRODUCTION.....	1
1.1. Introduction .....	1
1.2. Objective.....	3
1.3. The scope of the research.....	3
1.4. Research Methodology.....	1
CHAPTER II.....	2
BACKGROUND AND LITERATURE REVIEWS .....	2
2.1 Density functional theory (DFT).....	2
2.1.1. History of DFT .....	2
2.1.2. The Exchange Correlation Approximation .....	4
2.1.3. The Hubbard U and Grimme dispersion corrections.....	5
2.1.4 The density of states (DOS).....	7

2.1.5 Plane wave basis set .....	8
2.1.6 Periodic boundary condition .....	8
2.2 Titanium Dioxide (TiO <sub>2</sub> ).....	9
2.3 Deactivation of TiO <sub>2</sub> .....	10
2.4 Coke formation.....	11
2.5 Oxygen vacancy.....	12
2.6 Phase Transformation.....	14
2.7 Literature reviews.....	14
CHAPTER III.....	18
COMPUTATIONAL DETAILS.....	18
3.1 The bulk geometry relaxation calculation.....	18
3.2 The surface geometry calculation.....	19
3.2.1. Perfect anatase and rutile surfaces.....	19
3.2.2. Defect anatase and rutile surfaces.....	21
3.2.3. The coke geometry relaxation calculation via C1, C2, and C3 .....	22
3.3 Gibb free energy changes ( $\Delta G_{\text{ads}}$ ) calculation of coke adsorption.....	23
3.4 The effect of Hubbard U correction.....	24
3.5 The effect of Grimme dispersion correction (DFT-D3).....	24
CHAPTER IV .....	26
Results and discussion.....	26
4.1 Coke adsorption on TiO <sub>2</sub> catalyst.....	26
4.1.1 The investigation of the exchange-correlation functions and the addition of Hubbard U term.....	27
4.1.2 The effect of Grimme dispersion correction (DFT-D3) .....	34

4.2 The effect of O-vac on coke formation on TiO <sub>2</sub> catalyst .....	39
4.2.1 The investigation of oxygen vacancy active site on defect TiO <sub>2</sub> surfaces	39
4.2.2 Coke evolution on O-vac A-TiO <sub>2</sub> (101) and R-TiO <sub>2</sub> (110) surfaces.....	40
4.3 Electronic properties of coke on perfect and O-vac TiO <sub>2</sub> surfaces .....	43
4.3.1 Bader charge and charge density difference analysis .....	43
4.3.2 Projected density of states (PDOS) analysis.....	47
4.4 The effect of temperature on coke formation on TiO <sub>2</sub> surfaces.....	52
CHAPTER V .....	54
Conclusion .....	54
APPENDICES.....	55
REFERENCES .....	62
VITA.....	68



## LIST OF TABLES

	Page
Table 1 Literature review of anatase and rutile structures calculated in a set of U values (eV).....	20
Table 2 The bond distances (d) of the Ti-O atom at the active site of O1 on A-TiO <sub>2</sub> (101) and at the active site of O1 and O2 on R-TiO <sub>2</sub> (110) surfaces of coke adsorption in GGA and LDA methods with various U (0, 4, 5, and 6 eV).....	32
Table 3 The bond distances (d) of the Ti-O atom at the active site of O1 on A-TiO <sub>2</sub> (101) and at the active site of O1 and O2 on R-TiO <sub>2</sub> (110) surfaces of coke adsorption in GGA-D3 method with various U (0, 4, 5, and 6 eV).....	37
Table 4 Formation energies, in eV, of O-vac defects at different surface sites of A-TiO <sub>2</sub> (101) and R-TiO <sub>2</sub> (110).....	40
Table 5 The bond distance (d) between active site and Coke adsorption on A-TiO <sub>2</sub> (101) and R-TiO <sub>2</sub> (110) surfaces.....	43

## LIST OF FIGURES

	Page
Figure 1 The three mains caused to the deactivation of TiO <sub>2</sub> catalyst.....	3
Figure 2 Schematic representation of the ideal of periodic boundary condition [26]...	9
Figure 3 Periodic boundary conditions to represent actual systems with various supercells [25].....	9
Figure 4 The crystal structures of (a) rutile, (b) anatase, and (c) brookite [28].....	10
Figure 5 Formation and transformation of carbon on metal transition (a and s refer to adsorbed and solid states, respectively) [31] .....	12
Figure 6 A proposed band structure model for A-TiO <sub>2</sub> with oxygen vacancy [35] .....	13
Figure 7 A proposed band structure model for R-TiO <sub>2</sub> with oxygen vacancy [36] .....	13
Figure 8 The bulk structures of TiO <sub>2</sub> in (a) the A-TiO <sub>2</sub> and (b) R-TiO <sub>2</sub> phases .....	18
Figure 9 The surface structures of TiO <sub>2</sub> in perfect (a) A-TiO <sub>2</sub> (101) and (b) R-TiO <sub>2</sub> (110) surfaces.....	19
Figure 10 The possible active sites in top view on slab models of the perfect (a) A-TiO <sub>2</sub> (101) and (b) R-TiO <sub>2</sub> (110) surfaces .....	21
Figure 11 The slab models in top view with possible oxygen vacancy active sites of (a) the A -TiO <sub>2</sub> (101) and (b) the R-TiO <sub>2</sub> (110) surfaces.....	21
Figure 12 The possible active sites of carbon adsorption in top view on slab models in top view of defect on (a) the A-TiO <sub>2</sub> (101) and (b) the R-TiO <sub>2</sub> (110) surfaces .....	22
Figure 13 The optimized coke structure of (a) atomic coke (C1), (b) dimer coke (C2), and (c) trimer coke .....	23
Figure 14 All stable configurations of C1 adsorption on A-TiO <sub>2</sub> (101) surface in GGA method .....	27

Figure 15 All stable configurations of C1 adsorption on R-TiO <sub>2</sub> (110) surface in GGA method .....	27
Figure 16 The most stable adsorption configuration of C1, C2, and C3 on A-TiO <sub>2</sub> (101) surface in LDA+U method .....	29
Figure 17 The most stable adsorption configuration of C1, C2, and C3 on A-TiO <sub>2</sub> (101) surface in GGA+U method.....	30
Figure 18 The most stable adsorption configuration of C1, C2, and C3 on R-TiO <sub>2</sub> (110) surface in LDA+U method .....	31
Figure 19 The most stable adsorption configuration of C1, C2, and C3 on R-TiO <sub>2</sub> (110) surface in GGA+U method.....	31
Figure 20 The most stable adsorption configuration of C1, C2, and C3 on A-TiO <sub>2</sub> (101) surface in GGA+U-D3 method.....	36
Figure 21 The most stable adsorption configuration of C1, C2, and C3 on R-TiO <sub>2</sub> (110) surfaces in GGA+U-D3 method .....	37
Figure 22 The most stable adsorption configuration of C1, C2, and C3 on A-TiO <sub>2</sub> (101) surface in GGA+U4-D3 method and R-TiO <sub>2</sub> (110) surface in GGA+U6-D3 method.....	39
Figure 23 The slab models in top view with the possible oxygen vacancy sites on (a) the A -TiO <sub>2</sub> (101) and (b) the R-TiO <sub>2</sub> (110) surfaces.....	40
Figure 24 All stable configurations of C1 adsorption on O-vac A-TiO <sub>2</sub> (101) surface in GGA method .....	41
Figure 25 All stable configurations of C1 adsorption on O-vac R-TiO <sub>2</sub> (110) surface in GGA method .....	41
Figure 26 The most stable adsorption configuration of C1, C2, and C3 on O-vac A-TiO <sub>2</sub> (101) surfaces in GGA+U4-D3.....	42
Figure 27 The most stable adsorption configuration of C1, C2, and C3 on R-TiO <sub>2</sub> (110) surfaces in GGA+U6-D3.....	43

Figure 28 The charge density difference of C1, C2 and C3 adsorption on A-TiO <sub>2</sub> (101) in GGA+U4-D3 method are shown in yellow and pink regions as electron depletion and electron accumulation, respectively. The electron gain (-) and loss (+) with an isovalue of $\pm 0.017  e /\text{\AA}$ .....	44
Figure 29 The charge density difference of C1, C2 and C3 adsorption on R-TiO <sub>2</sub> (110) in GGA+U6-D3 method are shown in yellow and pink regions as electron depletion and electron accumulation, respectively. The electron gain (-) and loss (+) with an isovalue of $\pm 0.017  e /\text{\AA}$ .....	45
Figure 30 The charge density difference of C1, C2 and C3 adsorption on O-vac of A-TiO <sub>2</sub> (101) and R-TiO <sub>2</sub> (110) surfaces are shown in yellow and pink regions as electron depletion and electron accumulation, respectively. The electron gain (-) and loss (+) with an isovalue of $\pm 0.017  e /\text{\AA}$ .....	47
Figure 31 The projected density of state (PDOS) of perfect A-TiO <sub>2</sub> (101) and R-TiO <sub>2</sub> (110) surfaces in various methods .....	49
Figure 32 The projected density of state (PDOS) of C1, C2, and C3 adsorption on A-TiO <sub>2</sub> (101) and O-vac A-TiO <sub>2</sub> (110) in GGA+U4-D3 method .....	50
Figure 33 The projected density of state (PDOS) of C1, C2, and C3 adsorption on R-TiO <sub>2</sub> (110) and O-vac R-TiO <sub>2</sub> (110) in GGA+U6-D3 method .....	51
Figure 34 The Gibbs free energy changes ( $\Delta G_{\text{ads}}$ ) of coke adsorption on A-TiO <sub>2</sub> (101) and O-vac A-TiO <sub>2</sub> (101) surfaces in Different temperature (°C) .....	52
Figure 35 The Gibbs free energy changes ( $\Delta G_{\text{ads}}$ ) of coke adsorption on R-TiO <sub>2</sub> (110) and O-vac R-TiO <sub>2</sub> (110) surfaces in Different temperature (°C) .....	53

## CHAPTER I

### INTRODUCTION

#### 1.1. Introduction

Catalyst deactivation is a well-recognized phenomenon in the petroleum and chemical catalytic industries, such as oil refining, pollution control, and organic synthesis. The catalyst deactivation is unavoidable for most processes, these consequences may be avoided, postponed, or even reversed. Also, the industry costs for catalyst replacement or shutdown of the process required huge investment. Accordingly, understanding the root causes of the deactivation is an important factor for enhancing catalyst efficiency and preventing undesirable failures to minimize future catalyst deactivation [1, 2]. After decades of research, the heterogeneous catalysts such as metal oxides, such as  $\text{Al}_2\text{O}_3$ ,  $\text{SiO}_2$ ,  $\text{TiO}_2$ ,  $\text{ZnO}$ , and  $\text{ZrO}_2$  etc. [3], were recently used in many processes, including dehydrogenation, deoxygenation, water gas shift, hydrodesulphurization, and thermal catalytic decomposition, as these catalysts have interesting physicochemical and economical properties. Regarding the thermochemical process,  $\text{TiO}_2$  (titanium dioxide or titania) is a great metal oxide catalyst as a strong metal that encourage the interaction, including acid–base property, and chemical stability compared to other metal oxides.  $\text{TiO}_2$  has several advantages for low toxicity, earth abundance, corrosion resistance, high surface area, thermal and chemical stability [4].  $\text{TiO}_2$  exists in three important crystalline forms, including anatase (A- $\text{TiO}_2$ ), rutile (R- $\text{TiO}_2$ ) and brookite (B- $\text{TiO}_2$ ). The anatase and rutile are the most common types. The rutile has a larger crystalline size and its more stable than anatase phase. The most common polymorph of anatase and rutile are the 101 and 110 planes, respectively, due to its lower surface energies [5]. Many researchers revealed that anatase started to transform to rutile at  $600^\circ\text{C}$  and the rutile is stable when the temperature above  $800^\circ\text{C}$ . For the brookite is an orthorhombic structure, the third structure, which is metastable and usually converted to anatase and rutile when the temperature is raised to  $500^\circ\text{C}$  during the reactions [6]. Therefore, the brookite phase is rarely utilized.

Lee Eng Oi *et al.* investigated the TiO<sub>2</sub> in mesoporous, which calcined at the temperature (400-800°C) in the deoxygenation of triolein. The results showed the phase transformation of catalyst, changed anatase to rutile phase, including reduce the total acid amount of TiO<sub>2</sub> catalyst and enhance heavy carbon as coke on the surface [7]. Chun-Feng Li *et al.* studied the catalytic performance of defective TiO<sub>2</sub> catalyst in propane dehydrogenation (PDH) in both phases and the results showed that anatase is a good phase for PHD reaction. However, coke deposition will be generated when the concentration of oxygen vacancies (O-vacs) are increased, which influence to the PDH reaction and decrease the propane conversion[8]. These are related to the point that does coke formation, oxygen vacancy, and phase transformation affect the catalyst's deactivation.

In the 90s the DFT method was developed and has been widely applied in several systems [9] where standard DFT predicts delocalized solutions with experimental data . The two main types of exchange-correlation functionals that are extremely used are LDA and GGA functions. The various GGA function was continuously developed, such as PBE which developed by Perdew, Burke and Ernzerhof [10]. However, The failures of pure density functional methods of LDA or GGA could be corrected by introducing an additional U term which based on a simple Hubbard model and encourages the excess electronic charge localization, with the qualitative distribution depends on the value of U [11]. And another failure is the dispersion correction which could be corrected by using the Van der Waals (DFT-D3) for enhancing more specific and higher accuracy dispersion coefficients [12].

However, many U correction values have been investigated to find the appropriate on the electronic properties that close to the experiment as the DFT is a method to predict complex system behavior based on the model interactions between particles at an atomic scale in some way that the experiment difficulty explain. To prehension the effect of U values, which seem to observe in range 4 – 6 eV from many previous research works [9, 11, 13-17]. Moreover, the addition of the Grimme dispersion correction can help to improve those failures.

In this work,  $\text{TiO}_2$  has investigated its deactivation as a catalyst and to understand the effects of the Hubbard U correction in the range of 4 - 6 eV on its electronic properties with/without the DFT-D3 to understand relatives of coke formation, oxygen vacancy, phase transformation and the effect of temperature on coke adsorbed on surfaces in the range of 400-1000°C that affects the deactivation of catalyst to minimize future catalyst deactivation in different DFT methods.

## 1.2. Objective

To investigate the relatives of coke formation, oxygen vacancy and phase transformation that deactivates  $\text{TiO}_2$  on A- $\text{TiO}_2$  (101) and R- $\text{TiO}_2$  (110) surfaces in thermochemical processes via density functional theory (DFT).

## 1.3. The scope of the research

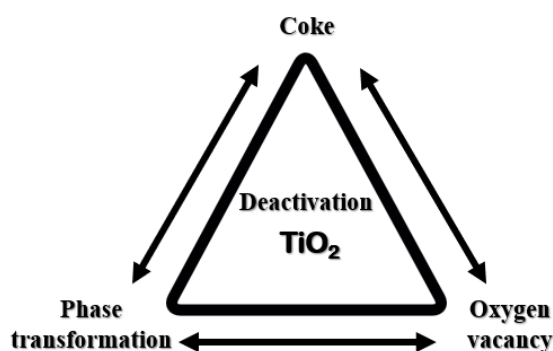


**Figure 1** The three mains caused to the deactivation of  $\text{TiO}_2$  catalyst

1.3.1. Study the deactivation by coke formation on  $\text{TiO}_2$  catalyst for thermochemical processes.

1.3.1.1. Study the effect of phase transformation from anatase to rutile  $\text{TiO}_2$  on coke formation including atomic (C1), dimer (C2), and trimer (C3) cokes.

1.3.1.2. Study the effect of oxygen-vacancy of anatase and rutile  $\text{TiO}_2$  on coke formation including C1, C2, and C3.

1.3.1.3. Compare coke formation of C1, C2, and C3 on defected anatase and rutile  $\text{TiO}_2$  surfaces.

1.3.2. Study the deactivation of catalyst with the effect of temperature on coke adsorbed on surfaces.

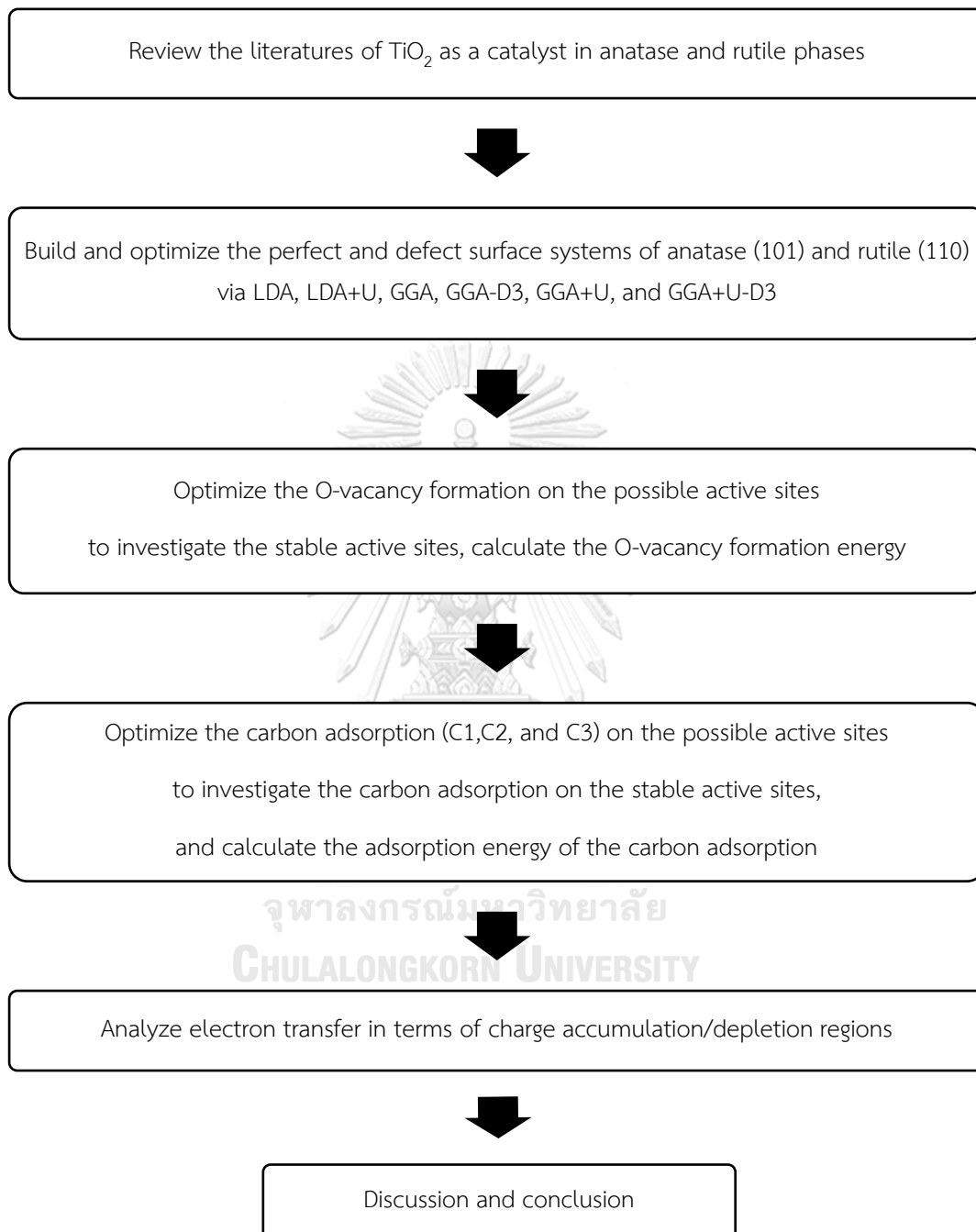
1.3.3. Study the effect of different exchange-correlation methods of LDA and GGA on electronic properties of  $\text{TiO}_2$  catalyst comparing to experimental investigation.

1.3.4. Study the effect of Van der Waals correction on coke on electronic properties and optimized geometries of coke on  $\text{TiO}_2$  surfaces.

1.3.5. Study the effect coulomb interaction energy  $U$  on the bandgap and the self-consistent on electronic properties of  $\text{TiO}_2$  surfaces.



#### 1.4. Research Methodology



## CHAPTER II

### BACKGROUND AND LITERATURE REVIEWS

#### 2.1 Density functional theory (DFT)

##### 2.1.1. History of DFT

In 1926, Erwin Schrödinger published the first famous wave equation, which is a mathematic equation to describe the physical properties of quantum phenomena and wave function movement as shown in the following equation below [18]

$$\hat{H}\Psi = E\Psi \quad (1)$$

where  $\hat{H}$ ,  $\Psi$ , and  $E$  are the Hamiltonian operator, the wave function, which the positions dependent on all electrons, and the energy of the system, respectively.

Even though, the wave function method has been successfully studied for small molecules' properties, which are unsuitable for studies of large system, extended solids. This function is also limiting to systems with a small number of electrons. Afterward, in 1927, Max Born and J. Robert Oppenheimer expanded a new approximation which is the Born-Oppenheimer approximation (BOA) from the Schrödinger's equation to describe the quantum behavior of the system of molecules because the mass of the nucleus ( $1.67 \times 10^{-27}$  kg) is much greater than the mass of the electron ( $9.1 \times 10^{-31}$  kg). Hence, the nucleus positions can be assumed fixed, and the wave function ( $\Psi$ ) depends only on electron positions ( $r$ ) as shown in the following equation (2):

$$\hat{H}(r)\Psi(r) = E\Psi(r) \quad (2)$$

However, this equation can solve only simple systems which is not able to complex systems. In 1964, Hohenberg and Kohn approached a functional that can solve the problem of finding the ground state energy of the electron in the external

potential. They presented that the ground-state total energy is a unique function of the electron density by developing the Schrödinger's equation. However, this function still limited for the definition that involved a set of 3N-dimensional trial wave functions which minimize the overall functionality. A year later, Kohn and Sham, who generated an idea to solve an iterative set of equations with a solution of a one-electron wave function that depends only on three spatial variables. The equation is referred to as the Kohn-Sham's equation, as shown below:

$$\left(-\frac{1}{2}\nabla^2 + v_{\text{eff}}(r) - \epsilon_j\right) \varphi_j(r) = 0 \quad (3)$$

with

$$v_{\text{eff}}(r) = v(r) + \int \frac{n(r')}{|r-r'|} dr' + v_{xc}(r) \quad (4)$$

where  $v(r)$  is the external potential,  $v_{xc}(r)$  is the exchange-correlation potential, and  $\epsilon_j$  is the Kohn-Sham's orbital of energy.

This function depends on the overall density function. Hence, this density needs to be known to define the effective potential then the equation can be solved. Also  $\varphi_j(r)$  is according to the  $j^{\text{th}}$ . The ground state density is given by:

$$n(r) = \sum_{j=1}^N |\varphi_j(r)|^2 \quad (5)$$

To solve equation 5. The  $\varphi_j(r)$  is used to generate to define the equations that are include self-consistent. In final, the ground state energy is given by:

$$E = \sum_j \epsilon_j + E_{xc}[n(r)] - \int v_{xc}(r)n(r)dr - \frac{1}{2} \int \frac{n(r)n(r')}{|r-r'|} dr'r \quad (6)$$

where  $E_{xc}[n(r)]$  is the exchange correlation energy. However, the exact form of the exchange correlation energy is still unknown [19].

### 2.1.2. The Exchange Correlation Approximation

The exchange correlation Approximation are extremely used in two main types DFT are the local density approximation (LDA) and the generalized gradient approximation (GGA).

First, LDA is used to estimate the density of the electron that has spatially uniform at all locations, but it seems to be work only in homogenous gas and a reasonable approximation for sluggardly varying densities. The LDA tends to predict in molecular, solid and semiconductor systems for the bandgap problem, as shown in the following equation (7):

$$E_{xc}^{LDA}[n(\mathbf{r})] = \int n(\mathbf{r})\epsilon_{xc}^{hom}[n(\mathbf{r})]d\mathbf{r} \quad (7)$$

where  $\epsilon_{xc}^{hom}[n(\mathbf{r})]$  is the exchange correlation energy per electron with electron density per volume of constant electron density ( $n$ ). However, the valence electron density in various bulk is not constant and unsuitable if its related to weak hydrogen bond or Van der Waals interaction. For the extension of local density functionals where the exact spin-scaling is known, this include electron spin must be considered as shown in the following equation (8):

$$E_{xc}^{LDA}[n_{\uparrow}, n_{\downarrow}] = \int n(\mathbf{r})\epsilon_{xc}[n_{\uparrow}, n_{\downarrow}]d^3\mathbf{r} \quad (8)$$

where  $\epsilon_{xc}(n_{\uparrow}, n_{\downarrow})$  is the exchange correlation energy per electron density ( $n_{\uparrow}, n_{\downarrow}$ ) in spin-polarized systems [10].

Second, GGA is a function that includes the gradient of non-uniformity electron density which depends not just on the value of the density at a point as in the LDA case. The GGA tends to predict in atoms, molecules, and solids. Hence, the more accurate exchange-correlation of GGA can capture local and semi-local exchange information, as shown in the following equation (9):

$$E_{xc}^{GGA}[n(\mathbf{r})] = \int n(\mathbf{r})\epsilon_{xc}[n(\mathbf{r}), \nabla n(\mathbf{r})] d\mathbf{r} \quad (9)$$

where  $\mathbf{n}(\mathbf{r})$  is the local electron density and  $\nabla\mathbf{n}(\mathbf{r})$  is the local gradient in the electron density. In case of the relative spin-polarization in term of the gradient of the density, this allows corrections to change the density away from the coordinate which can be written as follow [10]:

$$E_{xc}^{GGA}[\mathbf{n}_{\uparrow}, \mathbf{n}_{\downarrow}] = \int \mathbf{n}(\mathbf{r}) \varepsilon_{xc}[\mathbf{n}_{\uparrow}, \mathbf{n}_{\downarrow}, \nabla\mathbf{n}_{\uparrow}, \nabla\mathbf{n}_{\downarrow}] d^3\mathbf{r} \quad (10)$$

In 1992, The various GGA function was continuously developed, based on LDA by Perdew and Wang. This functional form is hugely used in DFT because it gives a good accuracy result by using a nonempirical system in uniformly electron gas. However, this application form is limited to procure inconstant of exchange correlation potential at low/high electron densities. Afterwards, there has the development of the method to PBE which developed by Perdew, Burke and Ernzerhof that identified elements with no empirical in GGA function. Also, the PBE function is very frequently exchange correlation potential at low/high electron densities.

### 2.1.3. The Hubbard U and Grimme dispersion corrections

However, based on the above information, the exchange correlation functionals still have limitation in the scription of the high correlation and on-site Coulomb interaction between electrons of the d and f states. Therefore, these corrections appear as a stage to improve those failures.

First, the Hubbard U correction is an approximate model which named by John Hubbard. This model was proposed in 1963, to describe the transition of electrons interaction on atomic orbitals in solids and this is recommended for analysis of electronic structure. The main effect of the U term is to move the d state toward more positive energies, which increases the band gap because the conduction state is narrowed. Then the Hubbard model is expressed to the Hubbard Hamiltonian ( $H_{Hub}$ ) to make it simpler which considered in two terms of the kinetic energy of the system ( $t$ ) and the on-site interaction of strength U (U) can be written as follows:

$$H_{\text{Hub}} = t \sum_{(i,j),\sigma} (c_{i,\sigma}^\dagger c_{j,\sigma} + \text{h.c.}) + U \sum_{\uparrow} n_{i,\uparrow} n_{i,\downarrow} \quad (11)$$

where (i,j) is nearest-neighbor atomic sites,  $c_{i,\sigma}^\dagger$ ,  $c_{j,\sigma}$  and  $n_{i,\sigma}$  are electronic creation, annihilation and number operators for electrons of spin  $\sigma$  on site  $i$  [20].

The general structure of the total energy using the LDA + U correction is provided can be written as follows:

$$E^{\text{LDA}+U} = E^{\text{LDA}} + \sum_I \left[ \frac{U^I}{2} \sum_{m,\sigma \neq m',\sigma'} n_m^{I\sigma} n_{m'}^{I\sigma'} - \frac{U^I}{2} n^I (n^I - 1) \right] \quad (12)$$

where  $n_m^{I\sigma}$  is the numbers of localized orbitals identified by the index  $m$  labels the localized states of the same atomic site  $I$ , and by the spin  $\sigma$  on site  $I$ , while  $n_m^{I\sigma} = n_{mm}^{I\sigma}$ , and  $n^I = \sum_{m,\sigma} n_m^{I\sigma}$ . And  $n_{m,m'}^{I\sigma}$  can be calculated by:

$$n_{m,m'}^{I\sigma} = \sum_{k,v} f_{kv}^\sigma \langle \psi_{kv}^\sigma | \phi_{m'}^I \rangle \langle \phi_m^I | \psi_{kv}^\sigma \rangle \quad (13)$$

where  $f_{kv}^\sigma$  is the coefficient the of Kohn-Sham's states (denoted as  $k$ -point, band, and spin indices),  $\psi_{kv}^\sigma$  is the projection of Kohn-Sham's orbitals, and  $(\phi_m^I)$  is the states of a localized basis set [20, 21].

The expression that provided the total energy for using the GGA + U correction was developed by Dudarev *et al* [22] can be written as follow:

$$E^{\text{GGA}+U} = E^{\text{GGA}} + \frac{(U-J)}{2} \left[ (\sum_j \rho_{jj}^\sigma) - (\sum_{j,i} \rho_{ji}^\sigma \rho_{ij}^\sigma) \right] \quad (14)$$

where  $U$  is the parameter of the local coulomb interaction between electron, and  $J$  is the parameter of local exchange interaction. The  $\rho_{jj}^\sigma$ ,  $\rho_{ji}^\sigma$ , and  $\rho_{ij}^\sigma$  are the electron density matrices of electrons in  $d$  orbital [22].

Second, the Grimme dispersion correction (DFT-D) is a method as a general tool for the computation of the dispersion energy in solid, molecules, and related electronic structure methods for large systems. The DFT-D promotes to increase the adsorption energy, this also can hold for Van der Waals in complex systems and for

the intramolecular noncovalent interactions that often appeared as problems. The DFT-D from Grimme is written as equation (15) and (16):

$$E_{\text{DFT-D}} = E_{\text{KS-DFT}} + E_{\text{disp}} \quad (15)$$

$$E_{\text{disp}} = \sum_{\text{AB}} \sum_{n=6,8,10,\dots} S_n \frac{C_n^{\text{AB}}}{r_{\text{AB}}^n} f_{\text{d},n}(r_{\text{AB}}) \quad (16)$$

where the  $E_{\text{KS-DFT}}$  determines the total energy by Kohn-Sham,  $C_n^{\text{AB}}$  is the dispersion coefficient in isotropic average of order  $n$  (denoted as  $n = 6, 8, 10, \dots$ ) of the pair AB atoms,  $S_n$  is the factor that depends on electron gradient and its density,  $r_{\text{AB}}$  is the internuclear distance between the pair AB atoms, and  $f_{\text{d},n}(r_{\text{AB}})$  is the damping function for DFT-D (N) (denoted as  $N = 1, 2, 3, \dots$ ) calculation type can be calculated by:

$$f_{\text{d},n}(r_{\text{AB}}) = \frac{1}{1 + 6(r_{\text{AB}} / (S_{r,n} R_0^{\text{AB}}))^{-\alpha_n}} \quad (17)$$

where  $S_{r,n}$  is the order-dependent scaling factor of the cutoff radii ( $R_0^{\text{AB}}$ ) and  $\alpha_n$  is the “steepness” parameter [12, 23].

#### 2.1.4 The density of states (DOS)

The density of states (DOS) is a system to describe the proportion of states that occupied by the system at each energy. The DOS in momentum space is derived from the number of waves confined to a box with a volume in  $D$  dimensions as  $V(D) = L^D$ . The length at each side of a box is  $L$ . For periodic boundary condition, the smallest component of the wavevector ( $\mathbf{k}$ ) is  $\frac{2\pi}{L}$ . The DOS can be defined as a function of wave number as equation 18:

$$\rho(\mathbf{k}) = \frac{1}{V(D)} \frac{dN(\mathbf{k})}{d\mathbf{k}} = s \left( \frac{1}{(2\pi)^D} \right) \Omega_D \mathbf{k}^{D-1} \quad (18)$$

where  $N(\mathbf{k})$  is the number of modes, the  $\Omega_D$  is expression for angular integrals in  $D$  dimensions, the  $s$  is the waves spin/polarization degree of freedom (if no phenomenon  $s = 1$  and  $s = 2$  for both electrons and photons). The units of DOS depend on the dimensionality [24].

#### 2.1.5 Plane wave basis set

Plane wave is one of basis wave functions that is the simplest and frequently, which commonly adopted in DFT method. This plane wave already functions as a solution for a free electron satisfying the Bloch Theorem and represents a smoothly varying function. The systematic of convergence and accuracy is possible with increase in the size of basis set. This plane wave is independent of the ionic (atomic) position because its nonlocal nature also calculates with other atom-centered basis set [25], The plane wave basis set ( $\phi_{PW}(\mathbf{r})$ ) can be determine as shown in equation 19:

$$\phi_{PW}(\mathbf{r}) = C \exp(i\mathbf{K} \cdot \mathbf{r}) \quad (19)$$

#### 2.1.6 Periodic boundary condition

The periodic boundary condition is widely used in particle-based simulation techniques and mathematical models for representing solid model. This used to represent a large (infinite) system by constructing a unit cell and super cell as a set of boundary condition and eliminate surface effects. The primary unit cell is just duplicated in all direction as shown in Figure 2. The actual calculation of periodic boundary condition can be taken place only in single unit cell (finite system) to represent image in super cell. The super cell can be extended to many systems under periodic boundary condition such as bulk, slab, cluster, and atom as shown in Figure 3. Therefore, the periodic boundary condition can be simulated to describe the actual solid behaviors.

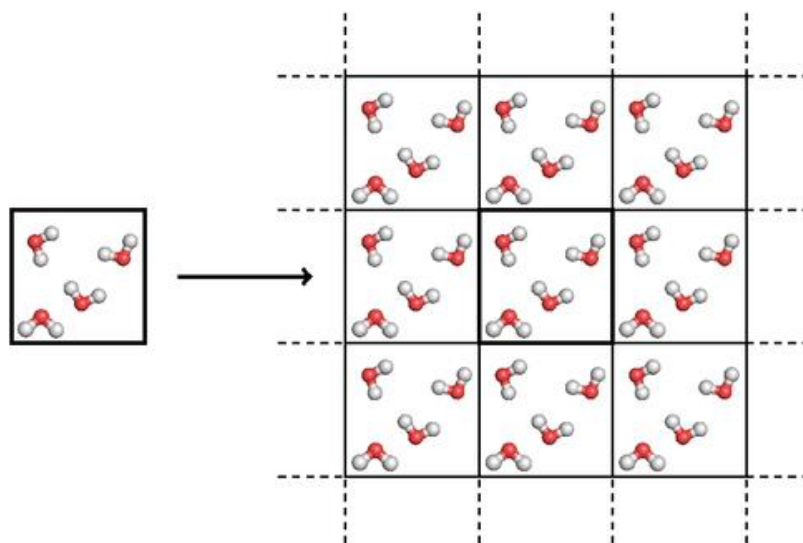


Figure 2 Schematic representation of the ideal of periodic boundary condition [26]

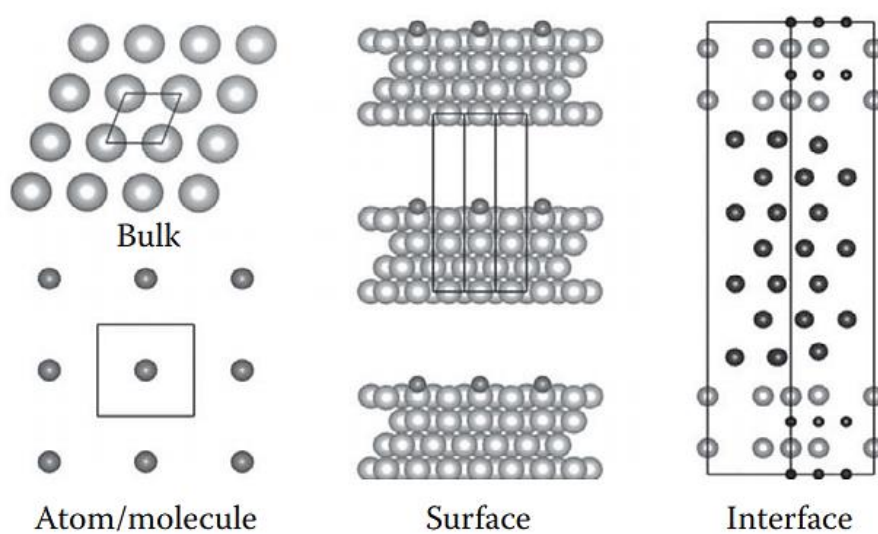
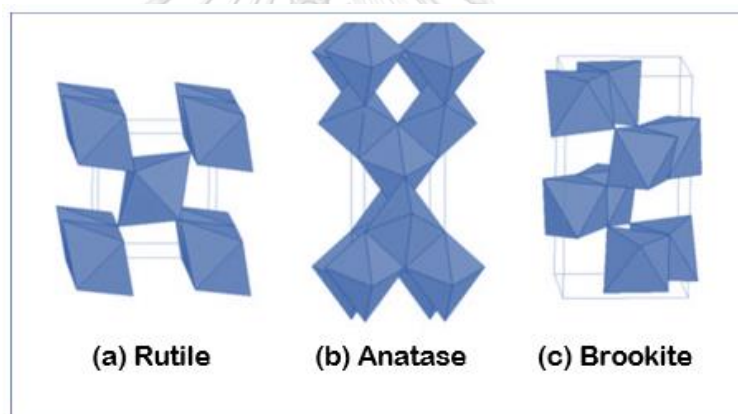


Figure 3 Periodic boundary conditions to represent actual systems with various supercells [25]

## 2.2 Titanium Dioxide ( $\text{TiO}_2$ )

Titanium dioxide (also known as titania,  $\text{TiO}_2$ ) is the model system in the surface science of transition metal oxides. This catalyst plays a crucial role in high stability in alkaline and acid media. The three main crystalline structures are widely studied, such as rutile, anatase, and brookite in Figure 4. Other crystalline phases of titania

have also been reported, for example,  $\text{TiO}_2$  (B), baddeleyite-like phase, columbite-like  $\text{TiO}_2$  (II), cotunnite-like OII phase, fluorite-like cubic phase, hollandite-like  $\text{TiO}_2$  (H), OI phase, and ramsdellite-like  $\text{TiO}_2$  (R). but those forms seem to be hard known oxides [27]. The two main forms (anatase and rutile) are the most common types, but the crystalline size of the rutile phase is larger. However, the anatase produced more active sites than rutile as it has the higher surface area, the amount of oxygen vacancies, the higher density of localized state that attributed towards slower charge carrier recombination [28]. For another form (Brookite) is an orthorhombic structure, which is rarely utilized, and rarely interested in most applications. Also, the rutile phase is the most thermal stable among the three phases. This catalyst shows merit in good photostability, low cost, environmental friendliness, high resistance toward corrosion, and easy availability.



**Figure 4** The crystal structures of (a) rutile, (b) anatase, and (c) brookite [28]

### 2.3 Deactivation of $\text{TiO}_2$

Accordingly, understanding the root causes of the deactivation is an important factor for enhancing catalyst efficiency and preventing undesirable failures to minimize future catalyst deactivation due to catalyst deactivation is inevitable in most processes, these consequences may be avoided, postponed, or even reversed. The deactivation of  $\text{TiO}_2$  can be caused by many things such as coke formation, oxygen vacancy, and phase transformation, which are mentioned in the next sections.

## 2.4 Coke formation

The formation of carbonaceous (coke or carbon) is involving hydrocarbons in side reaction or catalytic reactions and appeared on the catalyst which physically tend to cover the active site on the surface of catalyst. it may also deactivate the catalyst by pore blocking [1]. Qiu *et al.* have determined that the carbon structure of the coke are aliphatic carbon ( $C_{al}$ ) and aromatic carbon ( $C_{ar}$ ) which were estimated by the  $\gamma$  and  $\pi$  band (002) areas, respectively. The aromaticity ( $f_a$ ) was obtained from the equation (1), as shown in below by Lievens *et al.* [29], Sonibare, Haeger, and Foley [30].

$$f_a = \frac{C_{ar}}{(C_{ar}+C_{al})} = \frac{A_{\pi}}{(A_{\pi}+A_{\gamma})} \quad (20)$$

$$d_{002} = \frac{\lambda}{2 \sin \theta_{002}} \quad (21)$$

$$L_c = \frac{0.97\lambda}{(\beta_{002} \cos \theta_{002})} \quad (22)$$

$$L_a = \frac{1.84\lambda}{(\beta_{100} \cos \theta_{100})} \quad (23)$$

where  $d_{002}$ ,  $L_c$ ,  $L_a$ ,  $\lambda$ ,  $\beta$ ,  $\theta$  are the interlayer spacing, the average stacking height, the lateral size of the crystallite, the X-ray wavelength, the FWHM, and the corresponding scattering angle.

Mechanisms of carbon deposition and coke formation on metal transition catalysts for example from carbon monoxide (CO) and hydrocarbons are illustrated in Figure 5. The CO and hydrocarbons dissociate on metals to form an adsorbed atomic carbon ( $C_{\alpha}$ ), which can react to a polymeric carbon film ( $C_{\beta}$ ) and graphitic forms ( $C_c$ ). The  $C_{\alpha}$  can also react to vermicular carbon fibers ( $C_v$ ) or react with metal to form metal carbide ( $C_{\gamma}$ ) [31].

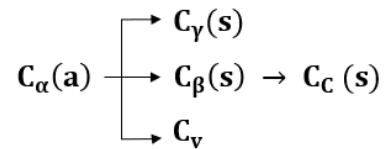
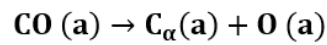
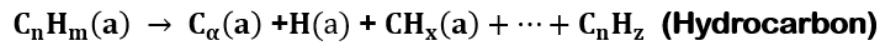
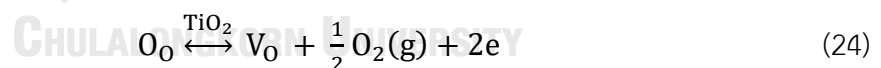


**Figure 5** Formation and transformation of carbon on metal transition (a and s refer to adsorbed and solid states, respectively) [31]

## 2.5 Oxygen vacancy

The oxygen vacancy (O-vac) is one of the most important among all the defects that identified on the TiO<sub>2</sub> catalyst. In many metal oxides, the O-vac is supposed to be the prevalent defect because the O-vac is relatively easier to generate, compared to Ti interstitial. In principle, the formation of oxygen vacancy on TiO<sub>2</sub> catalyst leads to form the Ti<sup>3+</sup> centers which are the unpaired electrons that could form in the electronic structure of the catalyst in donor levels [32]. However, the oxygen vacancy formation can be produced at elevated temperatures (>400°C) by annealing which described by the following equilibrium:



the equilibrium constant (K) of the reaction equation (24) determined by:

$$K = [V_0] n^2 p(O_2)^{(1/2)} \quad (25)$$

and the concentration of oxygen vacancies [V<sub>0</sub>] given by:

$$[V_0] = K n^{-2} p(O_2)^{-(1/2)} \quad (26)$$

where  $O_O$  is the oxygen lattice,  $V_O$  is the oxygen vacancy,  $[V_O]$  is the oxygen vacancy concentration, and  $p(O_2)$  is the oxygen pressure.

The oxygen vacancy involved the electronic property when the surface has been missing oxygen atom. The results showed the localization of one or two electrons at the oxygen vacancy state and the energetic cost of the oxygen vacancy formation is also minimized by forming a donor level below the conduction band in both anatase [32] and rutile [33] phases, in following Figure 6 and Figure 7. However, when compared the formation of oxygen vacancies on surface between anatase and rutile illustrate that the most stable surface of the A-TiO<sub>2</sub> (101) seems to have lower tendency of  $V_O$  than R-TiO<sub>2</sub> (110), because the A-TiO<sub>2</sub> (101) surface has lower stability of adjacent 4-fold Ti<sup>3p</sup> than 5-fold Ti<sup>3p</sup> on the R-TiO<sub>2</sub> (110) surface [34].

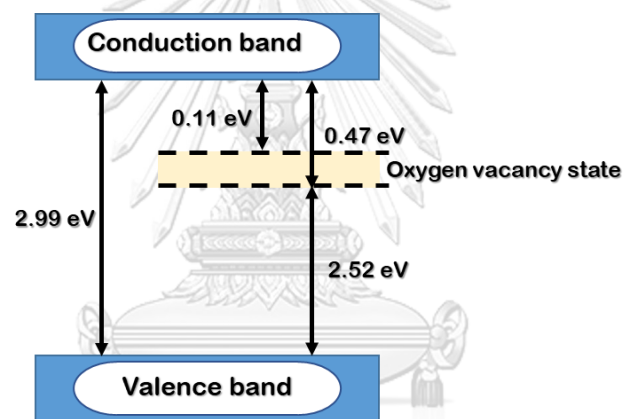


Figure 6 A proposed band structure model for A-TiO<sub>2</sub> with oxygen vacancy [35]

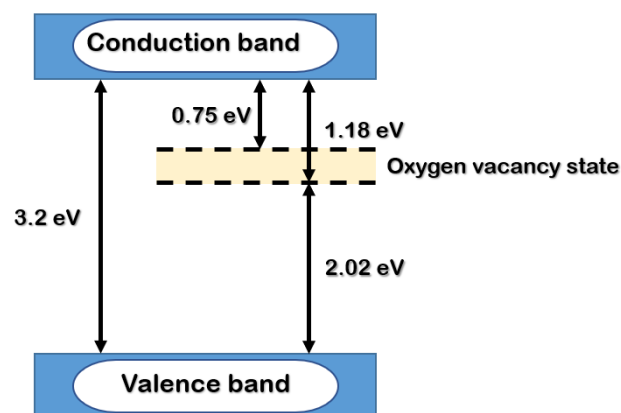


Figure 7 A proposed band structure model for R-TiO<sub>2</sub> with oxygen vacancy [36]

## 2.6 Phase Transformation

The phase transformation of anatase to rutile is considerable interest because the phase transformation may occur the properties (particle size, shape, and surface area etc.) and performances of process to be able to control or choose the right phase for any specific reactions. This is particularly for high temperature processes and applications. The generation of the TiO<sub>2</sub> phases depend significantly on the synthesis parameters, which are affect the product properties and performances. The kinetic of this process is considered in terms of time and temperature because the transformation of anatase to rutile is not instantaneous, it takes time for reconstructing [37]. Many researcher occurred that anatase started to transform to rutile at 600 – 800°C and completely changed to rutile when temperature reached to 900 – 1000°C [1, 38].

## 2.7 Literature reviews

Frederic Labat *et al.* [39] investigated the stable anatase and rutile TiO<sub>2</sub> surfaces using the DFT calculations in various methods, including LDA and GGA methods, by investigating the surface energy, which indicated the surface's activity. The surface energies of anatase (101) and (001) surfaces are 0.850 and 0.917 J/m<sup>2</sup>, respectively, for the LDA method and are 0.526 and 0.625 J/m<sup>2</sup>, respectively, for the GGA method. The surface energies of rutile (110), (100), and (001) surfaces are 0.906, 1.876, and 1.197 J/m<sup>2</sup>, respectively, for the LDA method and are 0.479, 1.393, and 0.694 J/m<sup>2</sup>, respectively, for the GGA method. The results showed that anatase (101) and rutile (110) are the most stable surfaces as these have the lowest surface energy for both LDA and GGA methods, which is why those surfaces are chosen as other works [40].

M.H. Samat *et al.* [41] studied the effect of Hubbard U calculations on optical properties of 3d on TiO<sub>2</sub> in bulk structure via DFT. They investigated the addition of U term due to the lack of self-interaction corrections local functional from LDA and

GGA can result in poor performance. Therefore, DFT+U approach can be used to treat the exchange-correlation functional. The results showed the U term has a strong effective on-site Coulomb repulsion among the localized Ti 3d electrons. In conclusion, The U term can provide a good optical behavior of TiO<sub>2</sub> which may be required to accurately describe the properties of the studied materials.

Gustavo Olinto da Silva, João B.L. Martins studied the effects of the Hubbard U term (at U = 0 – 9 eV.) and the Grimme dispersion correction (DFT-D2 and D3) on the benzene adsorption on the anatase TiO<sub>2</sub> (101) using the DFT calculations at GGA method with the PBE functional. The result shown the influence of the U term and dispersion correction on the electronic structure of the interaction processes was represented by the density of states (DOS). This illustrated that the U parameter can adjust the energy gap (E<sub>g</sub>) due to describing the interaction between electrons of the d state, while the DFT-D2 and D3 correction shown a large effect on adsorption energy by significantly increasing the adsorption energy [23].

Eduard Araujo-Lopez *et al.* [42] presented a study on the Hubbard term at 4.2 eV of U value and the Van der Waals dispersion in anatase (001) TiO<sub>2</sub> with an example of CO<sub>2</sub> adsorption molecule. For clean TiO<sub>2</sub> surface, the results showed the interatomic distances (Ti-O) of anatase (001) surface for GGA, GGA+U, and GGA+U+vdW were 1.948 Å, 1.954 Å, and 1.960 Å, respectively. To investigate the vdW dispersion, this revealed an elongation of Ti-O bonds at the TiO<sub>2</sub> surface slightly larger distance between layers. The adsorption energies for GGA+U and GGA+U+vdW are -1.377 eV and 1.528 eV, respectively, after the CO<sub>2</sub> adsorption. The O atom on the TiO<sub>2</sub> surface and the carbon atom are longer within the GGA+U+vdW approach. The inclusion of vdW dispersion improves the adsorption energy, resulting in a more stable structure and the agreement between the predicted and the experimental values of lattice parameters and interatomic distances. They suggested that including the Hubbard U and vdW corrections might be an accurate and efficient method to

describe the systems and vdW might give a correct description of the surface-molecule interaction.

From the point of the deactivation of  $\text{TiO}_2$  catalyst. Hongzhi Cheng and Annabella Selloni investigated the relative stabilities of oxygen vacancies at surface and subsurface sites of the A- $\text{TiO}_2$  (101) and R- $\text{TiO}_2$  (110) by using the DFT calculations at the generalized gradient approximation (GGA). These results indicated that at surface of both phases, the distribution of OV defects in A- $\text{TiO}_2$  (101) has higher concentration of defects than R- $\text{TiO}_2$  (110). Also, the calculations of O-vacancy diffusion pathways at A- $\text{TiO}_2$  (101) shown the energy hindrance to diffuse from the surface to subsurface sites is low to show a rapid equilibration of the vacancy distribution. These could explain why, the A- $\text{TiO}_2$  surfaces are found to have a significantly to be more difficult to reduce the defect concentration than those of R- $\text{TiO}_2$  (110) [43].

Mansour A. Al-Shafei *et al.* researched to understand the deactivation mechanism of  $\text{TiO}_2$  in the generated  $\text{SO}_2$  with the  $\text{H}_2\text{S}$  to produce sulfur and  $\text{H}_2\text{O}$  when the temperature reached to higher in the reactor. The results showed that increasing the temperature caused significantly changes the properties of the catalyst by phase transformation. The anatase started to transform to rutile phase during increasing temperature at  $800^\circ\text{C}$  caused to less catalyst activity and also found Hydrocarbon compounds on the surface which led to the deactivated catalyst [1]. Moreover, Lee Eng Oi *et al.* investigated the mesoporous  $\text{TiO}_2$  in the deoxygenation of triolein that calcined with hydrogen at different temperature ( $400\text{-}800^\circ\text{C}$ ). During the reaction, the temperature was raised to  $380^\circ\text{C}$  and maintained for 1-8 h, Further increasing of calcination temperatures distinctly transform the phase from anatase transformation to rutile and reduce the total acid amount of the  $\text{TiO}_2$  catalyst. The results showed anatase has a higher conversion and a higher medium strength acid site (anatase, mixed phase, rutile, in respectively) which produced a higher decarboxylation

selectivity and promoted a hydrocarbon in diesel range so the selectivity of heavy hydrocarbon for anatase was the lowest [7].

Chun-Feng Li *et al.* studied the catalytic performance of defective  $\text{TiO}_2$ -based catalysts for the propane dehydrogenation (PDH). The reaction temperature was pretreated at  $600^\circ\text{C}$  with a feed flow of air (air- $\text{TiO}_2$ -600) and  $\text{H}_2$  ( $\text{H}_2$ - $\text{TiO}_2$ -600). The results in all the  $\text{TiO}_2$  samples showed that anatase is a good phase for this reaction. To understand the nature of the PDH reaction, the process was proceeded in a long period and after 60 mins the air- $\text{TiO}_2$ -600 catalyst, showed coke deposition in the last stage of the reaction, and the propane conversion is also decreased. For  $\text{H}_2$ - $\text{TiO}_2$ -600 the results suggested that O-vacs were generated during thermal treatment with hydrogen. Moreover, at higher concentration of hydrogen can more easily react to the lattice oxygen of  $\text{TiO}_2$  to generate more O-vacs and the O-vacs also can promote the PDH reaction in turn to produce more hydrogen. However, there also has the relative of coke and O-vacs shown that coke will be generated when the concentration of O-vacs is higher, and leads to reduce the propane conversion [8].

Juchan Kim *et al.* investigated the coupling of methane to produce light hydrocarbons on the A- $\text{TiO}_2$  (101), which is the most stable plane surface of anatase surface by Plasma-Assisted Catalytic system. These methods can be used at room temperature and atmospheric pressure. The result shown the amount of coke deposition was greatly reduced, while the production of long chain hydrocarbons increased on titania active sites. The DFT calculations revealed that the coke was transformed into a more easily removable material from intermediate  $\text{CH}_x$  to the longer hydrocarbons in relative adsorption energy [44].

## CHAPTER III

### COMPUTATIONAL DETAILS

#### 3.1 The bulk geometry relaxation calculation

The bulk structures, as shown in Figure 8, should be mentioned that can be found in the work of Persson et al. by Materials Project. This work used DFT calculation for both anatase phase ( $I4_1/amd$  space group) and rutile phase ( $P4_2/mnm$  space group) have tetragonal crystal structure linked by a chain of  $TiO_6$  octahedra, and each unit cell contains six oxygen atoms around one Ti atom. The bulk structures were fully relaxed and initially computed using a planewave cutoff of 400 eV, grids of  $7 \times 7 \times 5$  and  $9 \times 9 \times 14$  k-points were used for integrating the total density of states (TDOS) calculations of anatase and rutile, respectively. Also set the other parameters such as force converged of  $0.01 \text{ eV/\AA}$ , energy convergence of  $1 \times 10^{-7} \text{ eV/atom}$ .

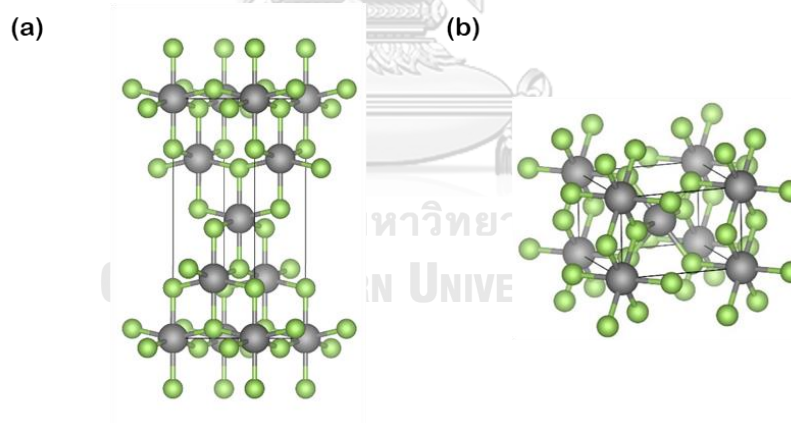


**Figure 8** The bulk structures of  $TiO_2$  in (a) the A- $TiO_2$  and (b) R- $TiO_2$  phases

### 3.2 The surface geometry calculation

#### 3.2.1. Perfect anatase and rutile surfaces

All structure models as shown in Figure 9, This work used DFT calculation also including the exchange-correlation functional from LDA-CA and GGA-PBE with/without the Van der Waals (DFT-D3) dispersion contribution and the Hubbard U parameter, such as LDA, LDA+U, GGA, GGA-D3, GGA+U, and GGA+U-D3.

The surface structures consisted of a 15 Å-vacuum-region along the z-axis to avoid interactions from the periodicity. The surface structures initially computed using grids of  $3 \times 3 \times 1$  k-points, slab of  $\text{TiO}_2$  layers with  $2 \times 2$  supercell for the A- $\text{TiO}_2$  (101) and R- $\text{TiO}_2$  (110) in the structural optimizations, the surface structures initially were computed in slabs of two  $\text{TiO}_2$  layers containing 48 atoms for the A- $\text{TiO}_2$  and three  $\text{TiO}_2$  layers containing 72 atoms for the R- $\text{TiO}_2$ . All atoms of the slab except those in the bottom layer were allowed to move. Also set the other parameters such as force converged of  $0.01 \text{ eV/\text{Å}}$ , energy convergence of  $1 \times 10^{-7} \text{ eV/atom}$ . However, the influence of the Hubbard U parameter with  $U = 4 - 6 \text{ eV}$  for both the anatase and rutile phases which corrected by other previous works, as shown in Table 1.

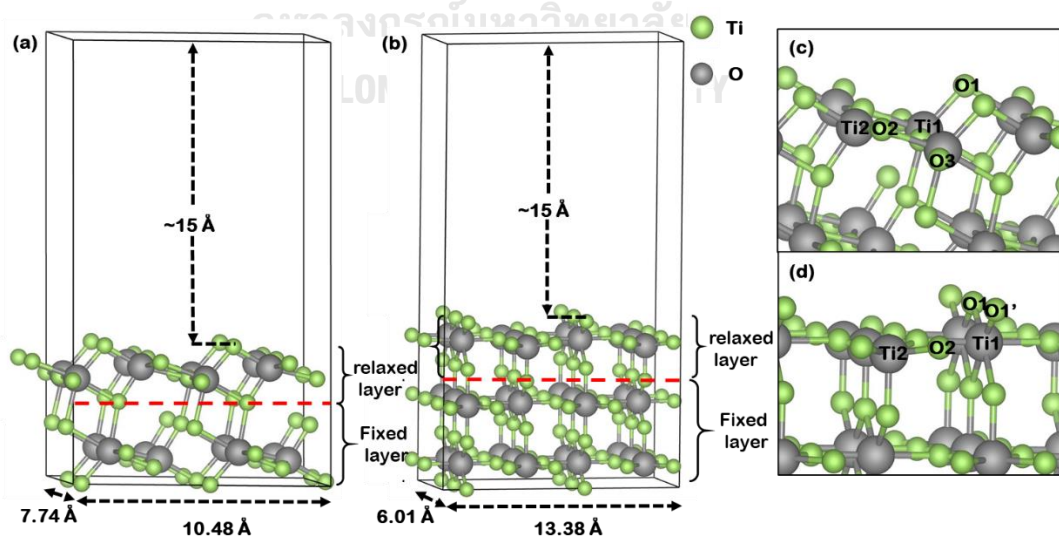


**Figure 9** The surface structures of  $\text{TiO}_2$  in perfect (a) A- $\text{TiO}_2$  (101) and (b) R- $\text{TiO}_2$  (110) surfaces

**Table 1** Literature review of anatase and rutile structures calculated in a set of U values (eV)

Polymorph	Method	U	Ref.
Anatase	PBE-GGA	4.0	[9]
	PBE-GGA	4.0	[13]
	PBE-GGA-D3	4.2	[42]
	PBE-GGA	4.2	[14]
	PBE-GGA-D3	4.2	[45]
	PBE-GGA-D3	4.2	[15]
	PW91-LDA	5.0	[15]
	PBE-GGA	5.0	[16]
	PBE-GGA	6.0	[46]
Rutile	PBE-GGA-D3	6.0	
	PBE-GGA	4.2	[11]
	PBE+GGA-D3	4.2	[45]
	PW91-GGA	4.5	[47]
	PW91-LDA	4.5	[15]
	PW91-LDA	5.0	[15]
	PBE-GGA	5.0	[48]
	PBE-LDA	5.0	[9]
	PBE-GGA	5.0	[17]
LDA	5.5		

3.2.1.1. All geometry of the possible active sites that carbon (C1, C2, and C3) can adsorb to determine the stable active sites of the perfect of A-TiO<sub>2</sub> (101) and R-TiO<sub>2</sub> (110) surfaces as shown in Figure 10. The possible active sites labeled as O (oxygen active sites), Ti (titanium active sites), H (hollow active sites), and B (bridge active sites), respectively.

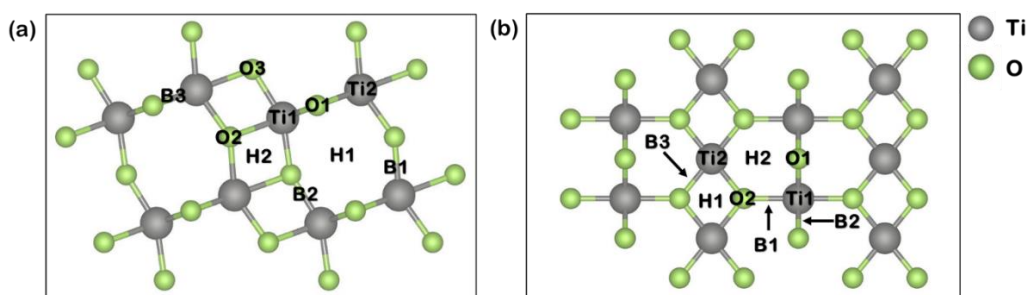


**Figure 10** The possible active sites in top view on slab models of the perfect (a) A-TiO<sub>2</sub>(101) and (b) R-TiO<sub>2</sub>(110) surfaces

### 3.2.2. Defect anatase and rutile surfaces

To build the defect surfaces, the possible oxygen vacancy active sites on defect A-TiO<sub>2</sub>(101) and R-TiO<sub>2</sub>(110) surfaces have been investigated to find a properly oxygen vacancy active site as shown in Figure 11. The possible oxygen vacancy active sites on the O-vac A-TiO<sub>2</sub>(101) are O1, O2, and O3, while O-vac R-TiO<sub>2</sub>(110) are O1 and O2.

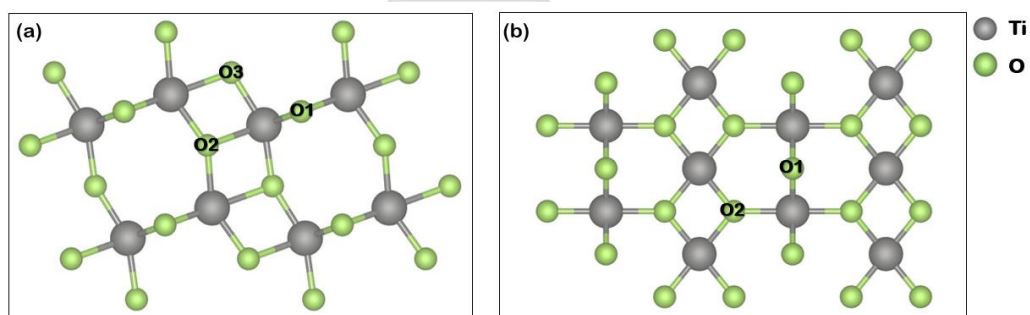


**Figure 11** The slab models in top view with possible oxygen vacancy active sites of (a) the A-TiO<sub>2</sub>(101) and (b) the R-TiO<sub>2</sub>(110) surfaces

The surface structures were built and investigated in all the possible active sites that carbon (C1, C2, and C3) can adsorb on the defect of the A-TiO<sub>2</sub>(101) and R-TiO<sub>2</sub>(110) surfaces in various method as LDA, LDA+U, GGA, GGA-D3, GGA+U, and GGA+U-D3 shown in Figure 10.

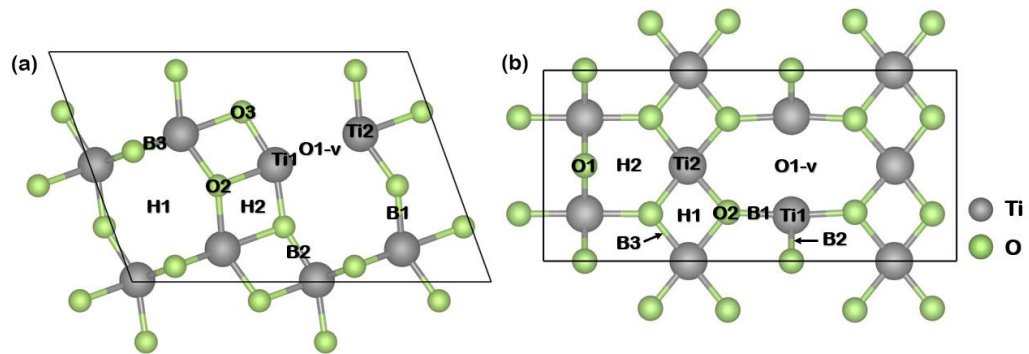


**Figure 12** The possible active sites of carbon adsorption in top view on slab models in top view of defect on (a) the A-TiO<sub>2</sub>(101) and (b) the R-TiO<sub>2</sub>(110) surfaces

### 3.2.2.1. Calculation the formation energy of oxygen vacancy ( $E_{\text{form}}$ )

The formation energy was determined from the equation (27):

$$E_{\text{form}} (\text{eV}) = E_{\text{O-vac}} - E_{\text{perfect}} + \frac{1}{2} E_{\text{O}_2} \quad (27)$$

where  $E_{\text{O}_2}$  is the total energy of O<sub>2</sub> molecules,  $E_{\text{O-vac}}$  is the total energy of the surface with defect, and  $E_{\text{perfect}}$  is the total energy of the surface without defect

### 3.2.3. The coke geometry relaxation calculation via C1, C2, and C3

The properties of isolated C1, C2, and C3 were calculated using a 15 × 15 × 15 Å cubic unit cell. All coke structures were built in box consist of a vacuum space in 15 Å to avoid the interaction between neighboring slabs. The force converged was set as 0.01 eV/Å, and energy convergence criteria was determined as 1×10<sup>-7</sup> eV/atom. The standard Monkhorst-Pack k-point sampling mesh was used to generate 3 × 3 × 3 grid and with cutoff energy of 400 eV. All adsorbed species were allowed to relax during the calculation. The structure of cokes as show in Figure 13.

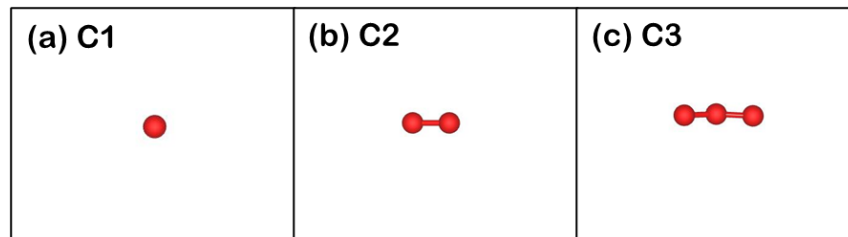


**Figure 13** The optimized coke structure of (a) atomic coke (C1), (b) dimer coke (C2), and (c) trimer coke

### 3.2.3.1. The adsorption energy analysis of coke adsorption

The adsorption energy ( $E_{\text{ads}}$ ) follows the equation (28):

$$E_{\text{ads}} \text{ (eV)} = E_{\text{complex}} - (E_{\text{coke}} + E_{\text{surface}}) \quad (28)$$

where  $E_{\text{complex}}$  is the total energy of the adsorption complex (C atom on catalyst surfaces),  $E_{\text{coke}}$  is the total energy of isolate coke in a vacuum, and  $E_{\text{surface}}$  is the total energy of the surfaces with and without defect.

### 3.3 Gibb free energy changes ( $\Delta G_{\text{ads}}$ ) calculation of coke adsorption

Gibbs free energy changes ( $\Delta G$ ) of carbon adsorption were calculated by

$$\Delta G_{\text{ads}} = G (C_i \text{ (ads)}) - G (\text{surface}) - G (C_i \text{ (gas)}) \quad (29)$$

where  $G (C_i \text{ (ads)})$  is the Gibbs free energy of carbon adsorbed species  $i$ ,  $G (\text{surface})$  is the Gibbs free energy of surface before carbon adsorption, and  $G (C_i \text{ (gas)})$  is the Gibbs free energy of isolate carbon species  $i$ . Furthermore, Gibbs free energy ( $G$ ) of carbon adsorption was calculated by

$$G_i = E_i + ZPE_i - RT \ln Q_{\text{vib}} \quad (30)$$

$$ZPE_i = \sum \frac{h\nu_i}{2} \quad (31)$$

$$Q_{\text{vib}} = \prod_1^n q_{\text{vib}_i} \quad (32)$$

$$q_{\text{vib}} = \frac{1}{(1 - e^{(-h\omega/K_B T)})} \quad (33)$$

where  $E_i$  is the total energy of species  $i$  provided from a normal DFT calculation,  $ZPE_i$  is the zero-point energy of adsorbed system, the gas constant ( $R$ ) is  $8.62 \times 10^{-5}$  eV  $K^{-1}$ ,  $Q_{\text{vib}}$  is the total vibrational partition function of adsorbed system in which the measurement from vibrational analysis, Planck's constant ( $h$ ) is  $4.14 \times 10^{-15}$  eV  $s^{-1}$ , the Boltzmann constant ( $K_B$ ) is  $8.617 \times 10^{-5}$  eV  $K^{-1}$ , vibrational frequency ( $\omega$ ,  $s^{-1}$ ), and the temperature ( $T$ ) in kelvin.

### 3.4 The effect of Hubbard U correction

The influence of Hubbard  $U$  term can be used to treat the exchange-correlation functional. In electronic properties of transition-metal systems with localized electrons, the  $U$  term attempts to induce the Coulomb repulsion, mainly within  $d$  orbitals of the Ti atom. The addition of  $U$  term effects on the structure of the  $TiO_2$  surface shows a contribution in the conduction band (CB) within the Ti  $3d$  orbitals while the O  $2p$  orbitals induce a contribution in the valence band (VB), which increase the bandgap of the  $TiO_2$  surface and narrow the conduction state to predict more accurate and in a good agreement with the experimental at the expense of small change in optimized geometry and surface energy. However, using a very large value of  $U$  can lead to mismatching, where the lattice parameters of  $TiO_2$  structure is increasing with increasing  $U$  due to the increasing of Coulomb repulsion [23, 49].

### 3.5 The effect of Grimme dispersion correction (DFT-D3)

The addition of DFT-D3 as the Van der Waals interaction can significantly increasing  $E_{\text{ads}}$  values and a separation distance between atoms on the surface and

adsorbed molecule as an elongation of Ti–O, Ti–C, and O–C bonds on the TiO<sub>2</sub> surface when considering interactions with external molecules. This is probably caused by the favoring of the formation of more localized states and the subsequent of electron repulsion between atoms on the surface [42, 50].



## CHAPTER IV

### Results and discussion

#### 4.1 Coke adsorption on TiO<sub>2</sub> catalyst

In this part, coke formation or coke adsorption on the catalyst surface is one of the parts to investigate the stability of the catalyst. The capability of coke formation was determined through the adsorption energy ( $E_{\text{ads}}$ ). The negative value of  $E_{\text{ads}}$  indicates featured interaction between carbon and catalyst surface. Moreover, the lower value of  $E_{\text{ads}}$  represents the stronger interaction between carbon and catalyst surface. In contrast, the higher value of  $E_{\text{ads}}$  represents a higher coke resistance.

To elucidate the interaction between cokes on A-TiO<sub>2</sub> (101) and R-TiO<sub>2</sub> (110) surfaces, each atomic (C1), dimer (C2), and trimer (C3) coke adsorptions are firstly investigated. All stable configurations of C1 adsorption on A-TiO<sub>2</sub> (101) and R-TiO<sub>2</sub> (110) surfaces are given in Figure 14 and Figure 15, respectively. The result shows the position of B3 active site, which is the most attractive or stable active site for adsorption that carbon should choose to adsorb as a first site. However, the other active sites with lower  $E_{\text{ads}}$  cannot be selected because after carbon is adsorbed on the catalyst surface, the catalyst surface is reconstructed as the position of Ti1 and H2 active sites that the oxygen is pushed out from the A-TiO<sub>2</sub> (101) surface.

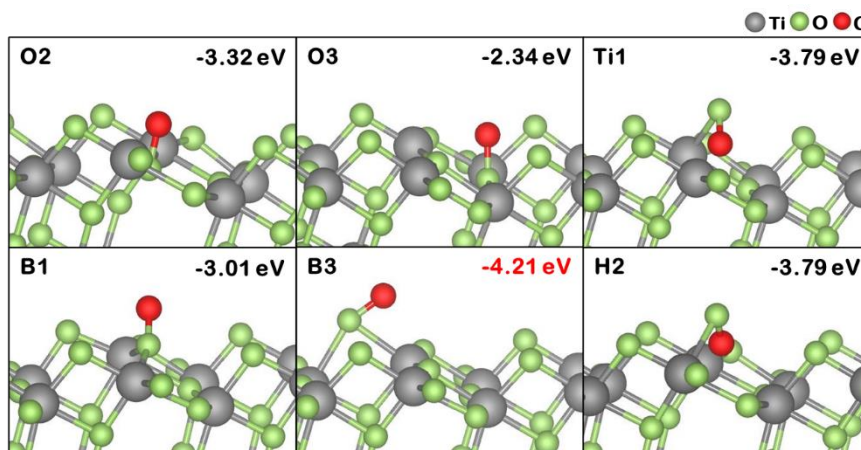


Figure 14 All stable configurations of C1 adsorption on A-TiO<sub>2</sub> (101) surface in GGA method

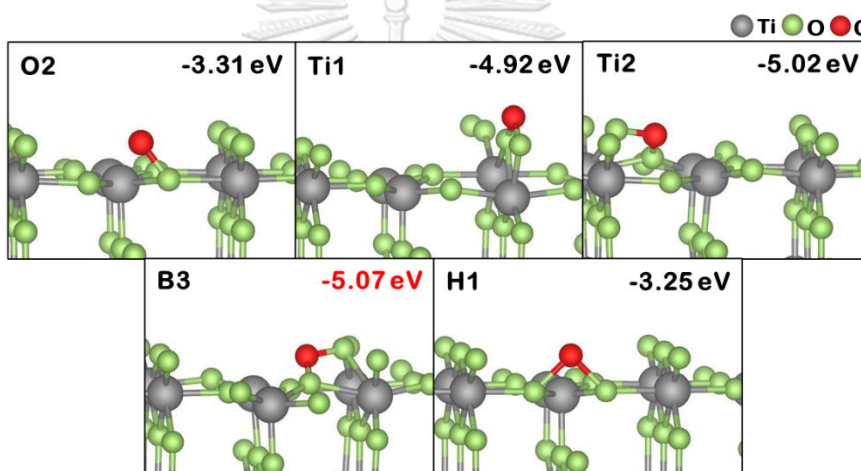


Figure 15 All stable configurations of C1 adsorption on R-TiO<sub>2</sub> (110) surface in GGA method

#### 4.1.1 The investigation of the exchange-correlation functions and the addition of Hubbard U term

To investigate the suitable method in this study, we analyzed the LDA and GGA method with the addition of Hubbard U (U) and dispersion corrections (D3) after examining the most stable active site above. The C1, C2 and C3 adsorption on A-TiO<sub>2</sub> (101) surface in LDA+U and GGA+U method which are given in Figure 16 and Figure 17, respectively, while Figure 18 and Figure 19 for the C1, C2 and C3 adsorption on R-TiO<sub>2</sub> (110). The  $E_{\text{ads}}$  of cokes on A-TiO<sub>2</sub> (101) and R-TiO<sub>2</sub> (110) surfaces corresponding

to the adsorption height in the LDA and GGA method that relate to  $U$  are summarized in Table 2.

For coke adsorption on A-TiO<sub>2</sub> (101) surface from Figure 16 and Figure 17, the  $E_{\text{ads}}$  of C1 at  $U = 0$  eV are -5.01 eV and -4.21 eV in LDA and GGA methods, respectively. The bond distances of the Ti1-O1 are 2.03 Å and 2.10 Å in LDA and GGA methods, respectively. For coke adsorption on R-TiO<sub>2</sub> (110) surface from Figure 18 and Figure 19, the  $E_{\text{ads}}$  of C1 at  $U = 0$  eV are -6.43 eV and -5.07 eV in LDA and GGA methods, respectively. The bond distances of the Ti1-O1 are 2.15 Å and 2.20 Å in LDA and GGA methods, respectively. The results showed that the  $E_{\text{ads}}$  of the LDA method has lower energy than GGA method because the electron density that has spatially uniform at all locations [51]. Moreover, the  $E_{\text{ads}}$  of the LDA method is more negative value than it should be, as in the realistic atomic model theory, while the GGA method is the gradient of non-uniformity electron density, which gives better accuracy result and more realistic with the atomic model theory.

For coke adsorption on A-TiO<sub>2</sub> (101) surface, the addition of  $U$  values in Figure 17 corresponding to the  $E_{\text{ads}}$  for coke adsorption on A-TiO<sub>2</sub> (101) surface in GGA+ $U$  method. The  $E_{\text{ads}}$  of C1 at  $U = 0, 4, 5,$  and  $6$  eV are -4.21, -4.38, -4.61, and -5.37 eV, respectively, as the  $E_{\text{ads}}$  is more negative, the interaction of bond between coke and surface is stronger. The results illustrate that  $U = 6$  eV has the lowest  $E_{\text{ads}}$ ; however, the C1 coke is found to consume the O1 active site on the A-TiO<sub>2</sub> (101) surface, forming a carbon monoxide (CO) molecule that desorbed at the end of the process as same as at  $U = 5$  eV, which after adsorbed C1, the structure of A-TiO<sub>2</sub> (101) surface changes. Therefore, the appropriate  $U$  value is 4 eV due to the structure has small change, but no breaking bond and the  $E_{\text{ads}}$  is still lower than without  $U$  value.

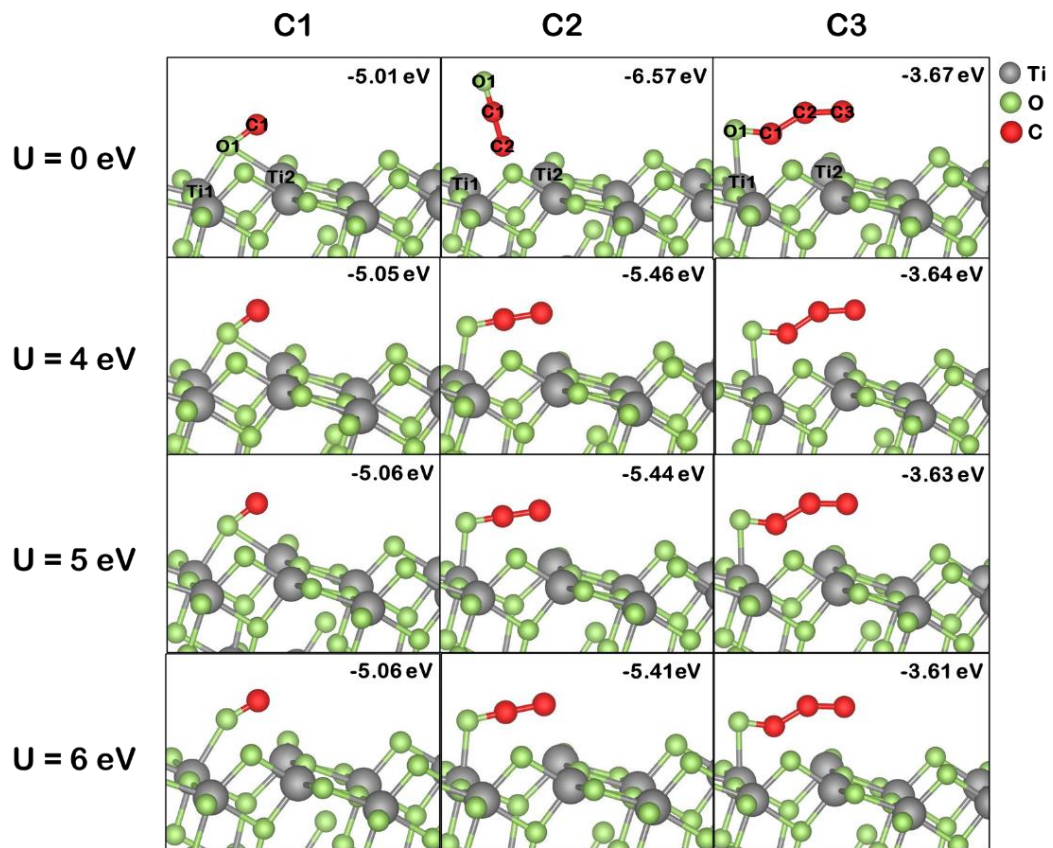
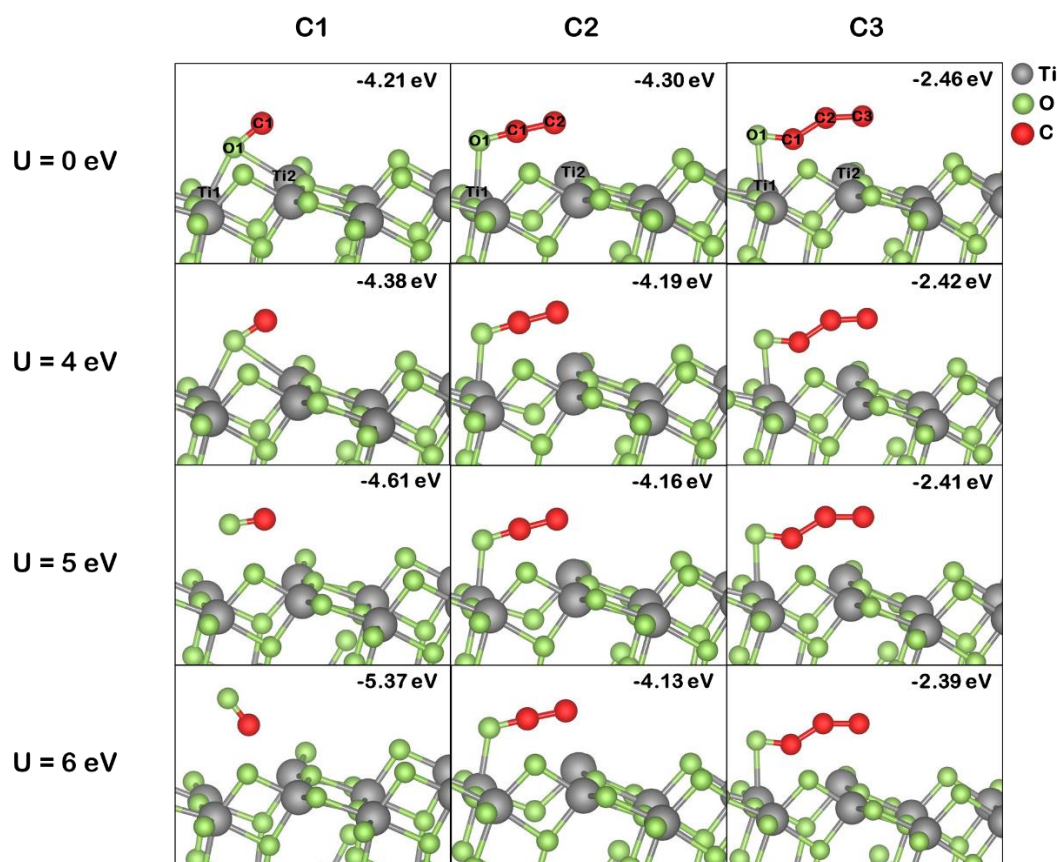


Figure 16 The most stable adsorption configuration of C1, C2, and C3 on A-TiO<sub>2</sub> (101) surface in LDA+U method



**Figure 17** The most stable adsorption configuration of C1, C2, and C3 on A-TiO<sub>2</sub> (101) surface in GGA+U method

For R-TiO<sub>2</sub> (110) surface in Figure 19, the  $E_{\text{ads}}$  of C1 at U = 0, 4, 5, and 6 eV are -5.07, -4.48, -4.50 and -4.56 eV, respectively. The results show at U = 6 eV has the lowest  $E_{\text{ads}}$  and the structure of R-TiO<sub>2</sub> (110) is more stable than other U values which is given the appropriate U value is at 6 eV. However, even at U = 0 eV has the  $E_{\text{ads}}$  lower than U 6 eV, adding U can encourages localization of the excess electronic charge which it can be expected to provide more accurate quantitative [49]. However, by applying U into the model of R-TiO<sub>2</sub> (110), the formation of CO is not observed unlike in the case of the A-TiO<sub>2</sub> (101).

For the increment of U, the  $E_{\text{ads}}$  is decreased on A-TiO<sub>2</sub> (101) while on R-TiO<sub>2</sub> (110), the  $E_{\text{ads}}$  is increased, and the bond distances also have no significance on both A-TiO<sub>2</sub> (101) and R-TiO<sub>2</sub> (110) surfaces for C2 and C3 adsorption while it seems effect to the bond distances with C1 adsorption.

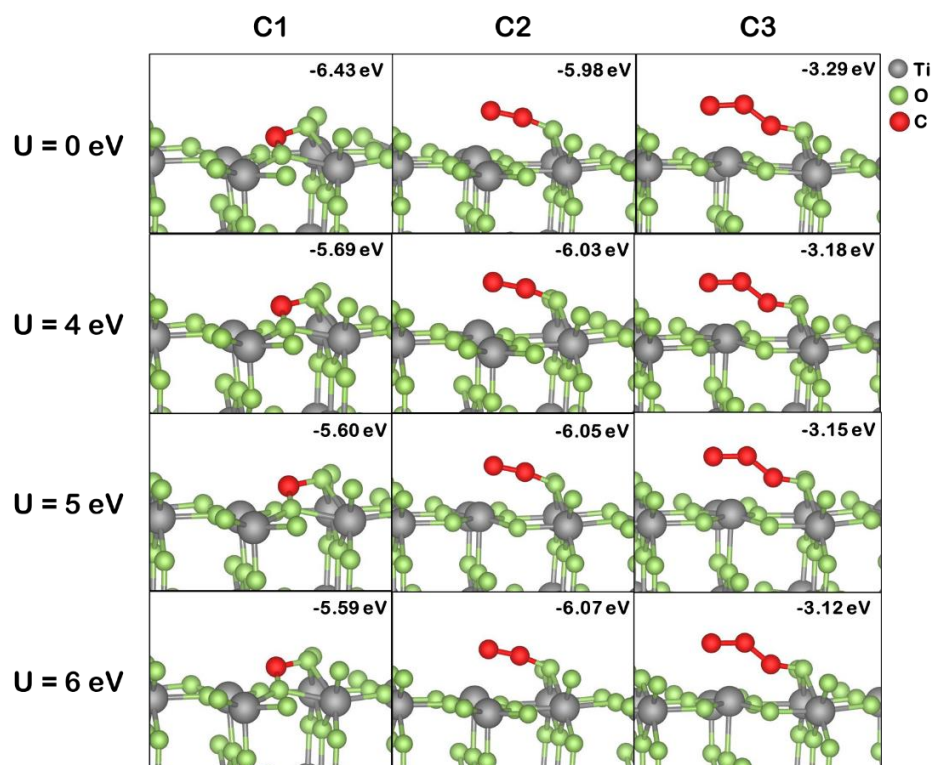


Figure 18 The most stable adsorption configuration of C1, C2, and C3 on R-TiO<sub>2</sub> (110) surface in LDA+U method

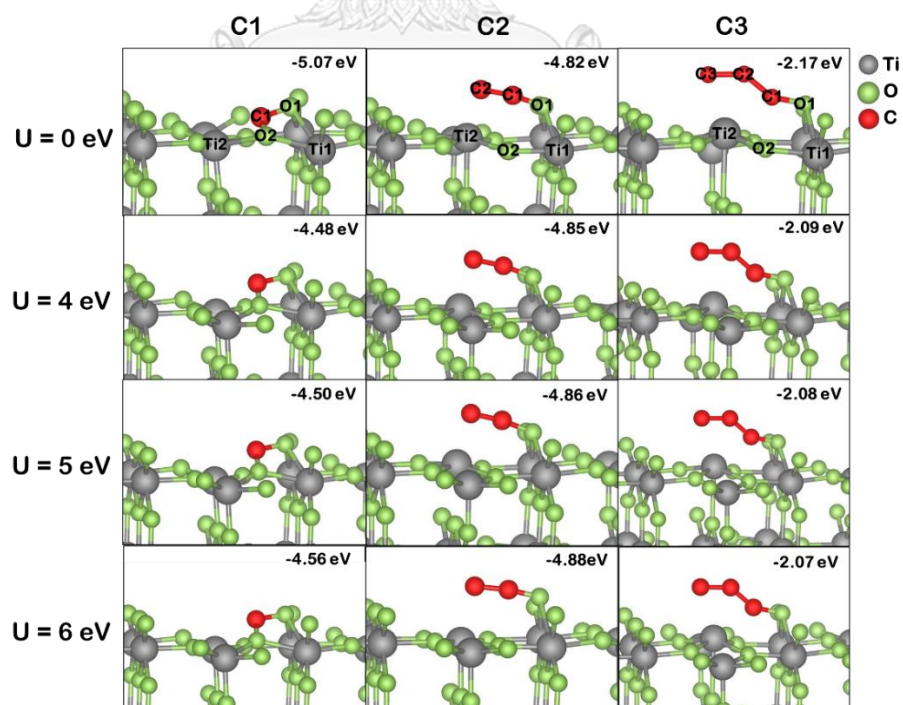


Figure 19 The most stable adsorption configuration of C1, C2, and C3 on R-TiO<sub>2</sub> (110) surface in GGA+U method

**Table 2** The bond distances ( $d$ ) of the Ti-O atom at the active site of O1 on A-TiO<sub>2</sub> (101) and at the active site of O1 and O2 on R-TiO<sub>2</sub> (110) surfaces of coke adsorption in GGA and LDA methods with various  $U$  (0, 4, 5, and 6 eV)

surface	absorbate	Method	$U$ (eV)	$d_{\text{Ti-O}}$ (Å)
A-TiO <sub>2</sub> (101)	C1	GGA	-	$d_{\text{Ti1-O1}} = 2.10$ $d_{\text{Ti12-O1}} = 2.23$
		GGA+U	4	$d_{\text{Ti1-O1}} = 2.28$ $d_{\text{Ti2-O1}} = 2.44$
			5	$d_{\text{Ti1-O1}} = 2.61$
			6	$d_{\text{Ti1-O1}} = 3.57$
		LDA	-	$d_{\text{Ti1-O1}} = 2.03$ $d_{\text{Ti12-O1}} = 2.21$
		LDA+U	4	$d_{\text{Ti1-O1}} = 2.06$ $d_{\text{Ti12-O1}} = 2.19$
			5	$d_{\text{Ti1-O1}} = 2.07$ $d_{\text{Ti12-O1}} = 2.19$
			6	$d_{\text{Ti1-O1}} = 2.20$
		C2	GGA	-
	GGA+U		4	$d_{\text{Ti1-O1}} = 2.09$
			5	$d_{\text{Ti1-O1}} = 2.09$
			6	$d_{\text{Ti1-O1}} = 2.09$
	LDA		-	$d_{\text{Ti1-O1}} = 3.99$
	LDA+U		4	$d_{\text{Ti1-O1}} = 2.03$
			5	$d_{\text{Ti1-O1}} = 2.04$
			6	$d_{\text{Ti1-O1}} = 2.04$
	C3		GGA	-
		GGA+U	4	$d_{\text{Ti1-O1}} = 2.18$
5			$d_{\text{Ti1-O1}} = 2.19$	
6			$d_{\text{Ti1-O1}} = 2.20$	
LDA		-	$d_{\text{Ti1-O1}} = 2.08$	

Table 2 Continued

surface	absorbate	Method	U (eV)	$d_{\text{Ti-O}}$ (Å)	
A-TiO <sub>2</sub> (101)	C3	LDA+U	4	$d_{\text{Ti1-O1}} = 2.11$	
			5	$d_{\text{Ti1-O1}} = 2.12$	
			6	$d_{\text{Ti1-O1}} = 2.13$	
R-TiO <sub>2</sub> (110)	C1	GGA	-	$d_{\text{Ti1-O1}} = 2.20$ $d_{\text{Ti1-O2}} = 2.14$ $d_{\text{Ti2-O2}} = 2.06$	
			GGA+U	4	$d_{\text{Ti1-O1}} = 2.22$ $d_{\text{Ti1-O2}} = 2.12$ $d_{\text{Ti2-O2}} = 2.10$
				5	$d_{\text{Ti1-O1}} = 2.23$ $d_{\text{Ti1-O2}} = 2.12$ $d_{\text{Ti2-O2}} = 2.11$
		6		$d_{\text{Ti1-O1}} = 2.23$ $d_{\text{Ti1-O2}} = 2.12$ $d_{\text{Ti2-O2}} = 2.12$	
		LDA	-	$d_{\text{Ti1-O1}} = 2.15$ $d_{\text{Ti1-O2}} = 2.13$ $d_{\text{Ti2-O2}} = 2.03$	
			LDA+U	4	$d_{\text{Ti1-O1}} = 2.15$ $d_{\text{Ti1-O2}} = 2.10$ $d_{\text{Ti2-O2}} = 2.05$
				5	$d_{\text{Ti1-O1}} = 2.16$ $d_{\text{Ti1-O2}} = 2.10$ $d_{\text{Ti2-O2}} = 2.07$
		6		$d_{\text{Ti1-O1}} = 2.17$ $d_{\text{Ti1-O2}} = 2.11$ $d_{\text{Ti2-O2}} = 2.09$	

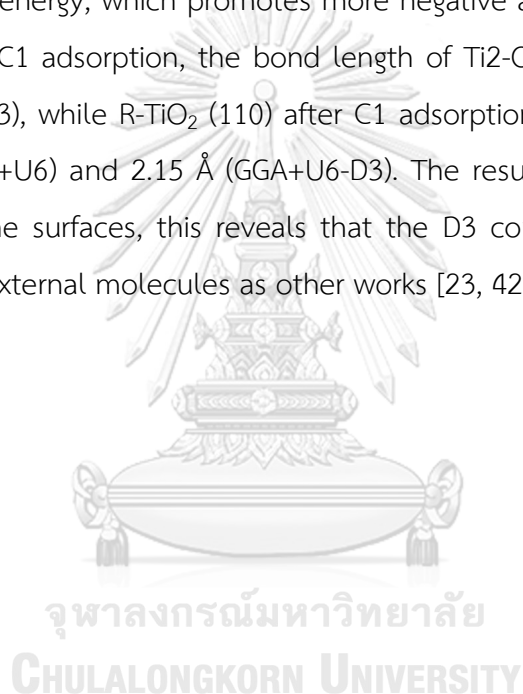
Table 2 Continued

surface	adsorbate	Method	U (eV)	$d_{\text{Ti-O}}$ (Å)	
R-TiO <sub>2</sub> (110)	C2	GGA+U	4	$d_{\text{Ti1-O1}} = 2.20$	
			5	$d_{\text{Ti1-O1}} = 2.20$	
			6	$d_{\text{Ti1-O1}} = 2.19$	
		LDA	-	$d_{\text{Ti1-O1}} = 2.17$	
		LDA+U	4	$d_{\text{Ti1-O1}} = 2.15$	
			5	$d_{\text{Ti1-O1}} = 2.14$	
			6	$d_{\text{Ti1-O1}} = 2.14$	
		C3	GGA	-	$d_{\text{Ti1-O1}} = 2.31$
				-	$d_{\text{Ti1-O1}} = 2.31$
	GGA+U		4	$d_{\text{Ti1-O1}} = 2.29$	
			5	$d_{\text{Ti1-O1}} = 2.28$	
			6	$d_{\text{Ti1-O1}} = 2.28$	
	LDA		-	$d_{\text{Ti1-O1}} = 2.22$	
	LDA+U	4	$d_{\text{Ti1-O1}} = 2.20$		
		5	$d_{\text{Ti1-O1}} = 2.20$		
6		$d_{\text{Ti1-O1}} = 2.19$			

#### 4.1.2 The effect of Grimme dispersion correction (DFT-D3)

The effect of D3 correction on stable adsorbed configuration is also investigated, which are given in Figure 20 for coke adsorption on A-TiO<sub>2</sub> (101), while in Figure 21 for coke adsorption on R-TiO<sub>2</sub> (110). The bond distance ( $d$ ) in the GGA method on A-TiO<sub>2</sub> (101) and R-TiO<sub>2</sub> (110) surfaces that relate to U and DFT-D3 are summarized in Table 3. The  $E_{\text{ads}}$  for C1 adsorption on A-TiO<sub>2</sub> (101) surface in GGA+U-D3 method at U = 0, 4, 5, and 6 eV are -4.33, -4.49, -4.71, and -5.44 eV, respectively, as the  $E_{\text{ads}}$  is more negative, the interaction of bond between coke and surface is stronger. However, the increment of U that higher than 4 eV, the C1 coke is still found to consume the O1 active site on the A-TiO<sub>2</sub> (101) surface, forming a CO molecule, which after adsorbed C1, the structure of A-TiO<sub>2</sub> (101) surface changes. For R-TiO<sub>2</sub> (110) surface in GGA+U-D3 method, the  $E_{\text{ads}}$  of C1 at U = 0, 4, 5, and 6 eV are -

5.15, -4.57, -4.68 and -4.74 eV, respectively. The results show that  $U\text{-D3} = 6$  eV has the lowest  $E_{\text{ads}}$ , and the structure of  $\text{R-TiO}_2$  (110) is more stable than other  $U$  values, which still make the  $U$  at 6 eV is the appropriate  $U$  value. However, even adding D3 term at  $U = 0$  eV has the  $E_{\text{ads}}$  lower than  $U$  6 eV due to the same mentioned reason as only  $U$  term and the formation of CO is also not observed as only  $U$  correction on  $\text{R-TiO}_2$  (110) surface. Thus, adding the D3 correction also has lower adsorption energy of the coke adsorption on both  $\text{A-TiO}_2$  (101) and  $\text{R-TiO}_2$  (110) surfaces due to it include the interaction between atoms [12]. The result revealed that the contributes to the adsorption energy, which promotes more negative adsorption energy [23]. For  $\text{A-TiO}_2$  (101) after C1 adsorption, the bond length of  $\text{Ti2-O1}$  is 2.44 Å (GGA+U4) and 2.98 Å (GGA+U4-D3), while  $\text{R-TiO}_2$  (110) after C1 adsorption, the bond length of  $\text{Ti2-O2}$  is 2.12 Å (GGA+U6) and 2.15 Å (GGA+U6-D3). The result shows an elongation of  $\text{Ti-O}$  bonds on the surfaces, this reveals that the D3 correction is considering the interactions with external molecules as other works [23, 42, 52]



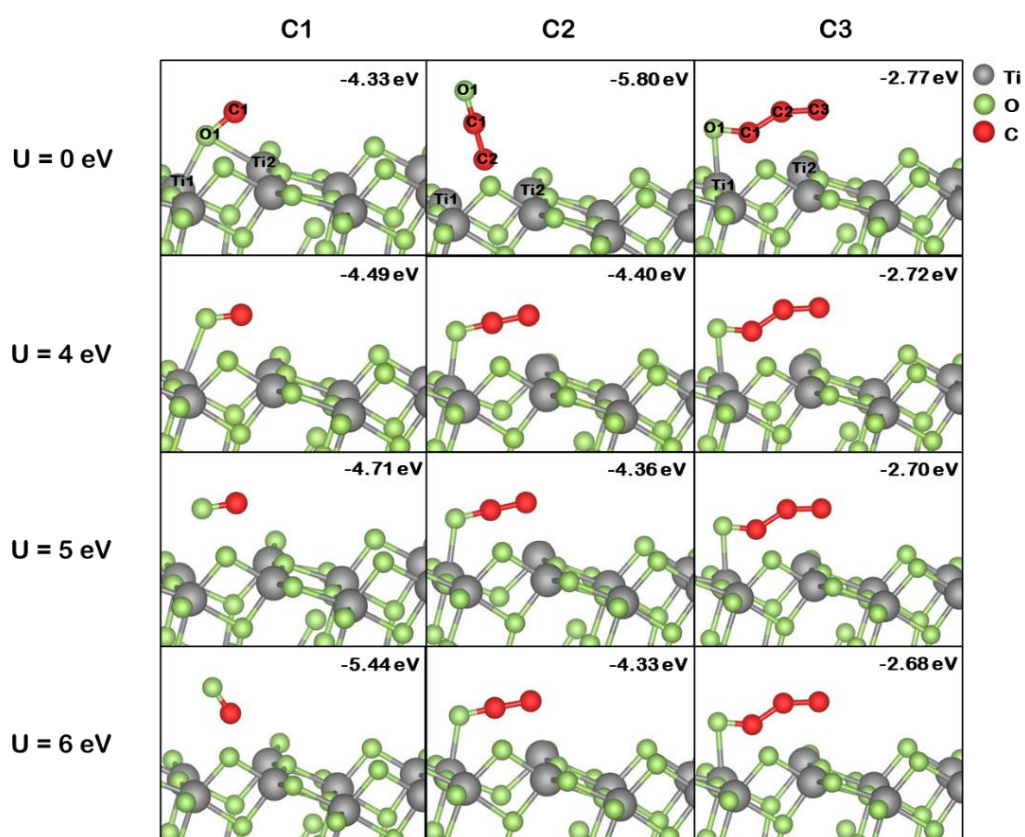
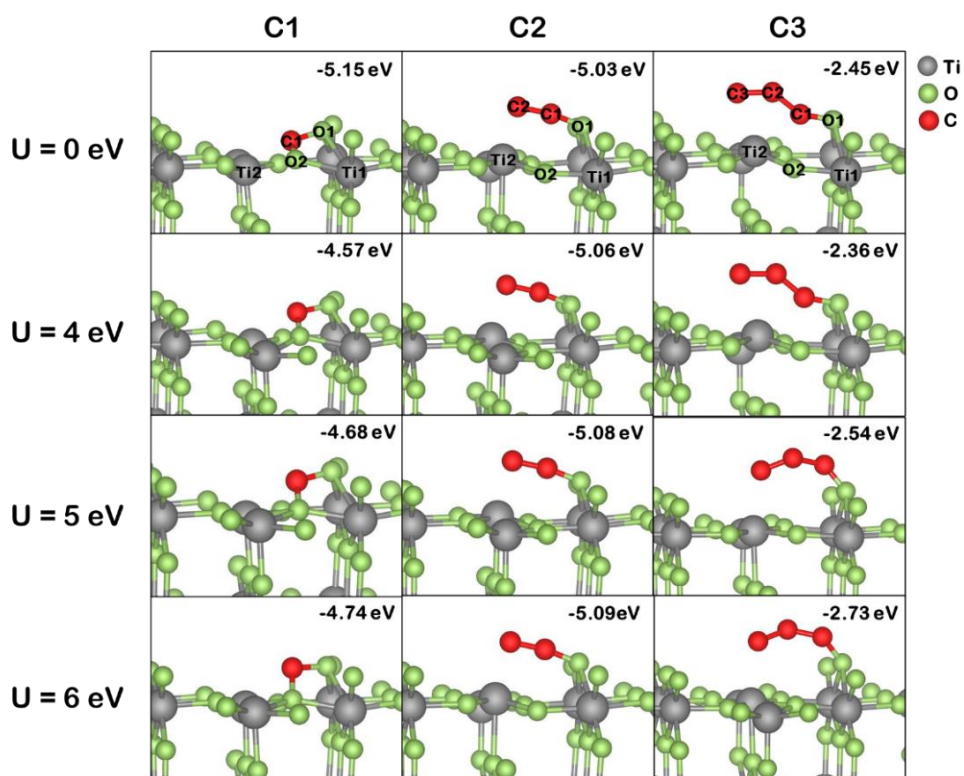


Figure 20 The most stable adsorption configuration of C1, C2, and C3 on A-TiO<sub>2</sub> (101) surface in GGA+U-D3 method



**Figure 21** The most stable adsorption configuration of C1, C2, and C3 on R-TiO<sub>2</sub> (110) surfaces in GGA+U-D3 method

**Table 3** The bond distances (*d*) of the Ti-O atom at the active site of O1 on A-TiO<sub>2</sub> (101) and at the active site of O1 and O2 on R-TiO<sub>2</sub> (110) surfaces of coke adsorption in GGA-D3 method with various U (0, 4, 5, and 6 eV)

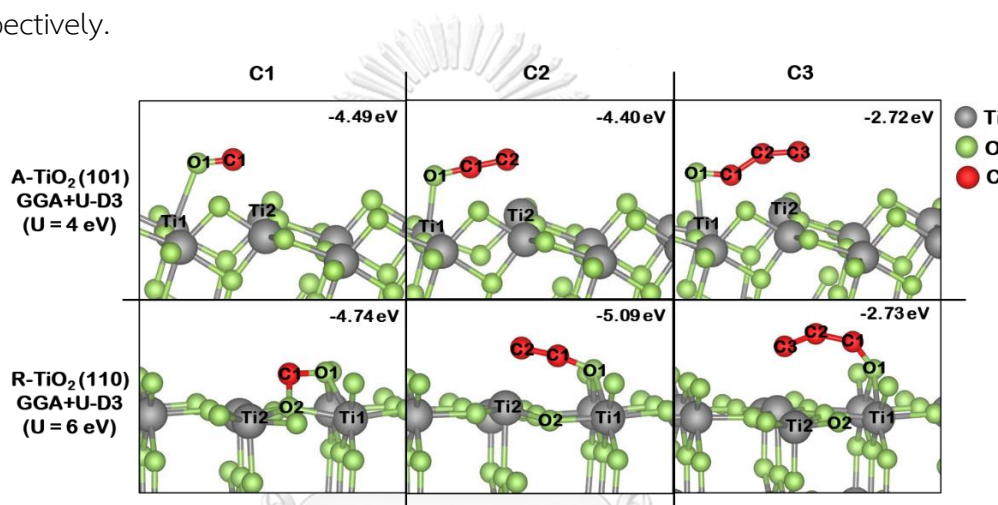
surface	absorbate	Method	U (eV)	$d_{\text{Ti-O}}$ (Å)
A-TiO <sub>2</sub> (101)	C1	GGA-D3	-	$d_{\text{Ti1-O1}} = 2.09$ $d_{\text{Ti12-O1}} = 2.23$
			GGA+U-D3	4
			5	$d_{\text{Ti1-O1}} = 2.56$
			6	$d_{\text{Ti1-O1}} = 3.47$
	C2	GGA-D3	-	$d_{\text{Ti1-O1}} = 4.03$
			GGA+U-D3	4
			5	$d_{\text{Ti1-O1}} = 2.09$
			6	$d_{\text{Ti1-O1}} = 2.09$

Table 3 Continued

surface	absorbate	Method	U (eV)	$d_{\text{Ti-O}}$ (Å)		
A-TiO <sub>2</sub> (101)	C3	GGA-D3	-	$d_{\text{Ti1-O1}} = 2.15$		
		GGA+U-D3	4	$d_{\text{Ti1-O1}} = 2.18$		
			5	$d_{\text{Ti1-O1}} = 2.19$		
			6	$d_{\text{Ti1-O1}} = 2.20$		
R-TiO <sub>2</sub> (110)	C1	GGA-D3	-	$d_{\text{Ti1-O1}} = 2.20$		
				$d_{\text{Ti1-O2}} = 2.14$		
				$d_{\text{Ti2-O2}} = 2.06$		
	GGA+U-D3	4	$d_{\text{Ti1-O1}} = 2.21$			
			$d_{\text{Ti1-O2}} = 2.12$			
			$d_{\text{Ti2-O2}} = 2.10$			
		5	$d_{\text{Ti1-O1}} = 2.25$			
			$d_{\text{Ti1-O2}} = 2.09$			
			$d_{\text{Ti2-O2}} = 2.13$			
		6	$d_{\text{Ti1-O1}} = 2.17$			
			$d_{\text{Ti1-O2}} = 2.05$			
			$d_{\text{Ti2-O2}} = 2.15$			
	C2	GGA-D3	-	$d_{\text{Ti1-O1}} = 2.23$		
				GGA+U-D3	4	$d_{\text{Ti1-O1}} = 2.20$
					5	$d_{\text{Ti1-O1}} = 2.19$
		6	$d_{\text{Ti1-O1}} = 2.19$			
C3		GGA-D3	-	$d_{\text{Ti1-O1}} = 2.30$		
				GGA+U-D3	4	$d_{\text{Ti1-O1}} = 2.28$
	5				$d_{\text{Ti1-O1}} = 2.27$	
6	$d_{\text{Ti1-O1}} = 2.28$					

In conclusion for this section, the most stable adsorption configuration of C1, C2, and C3 at U = 4 eV and U = 6 eV on A-TiO<sub>2</sub> (101) and R-TiO<sub>2</sub> (110) surfaces, respectively, are demonstrated in Figure 22. The enlargement of coke size on A-TiO<sub>2</sub>

(101), the bond distances of the Ti1-O1 at  $U = 4$  eV are 2.28 Å, 2.09 Å, and 2.18 Å for C1, C2, and C3, respectively. For R-TiO<sub>2</sub> (110), the bond distances of the Ti1-O1 at  $U = 6$  eV are 2.23 Å, 2.19 Å, and 2.28 Å for C1, C2, and C3, respectively. The results illustrated that C1 is strongly adsorbed on A-TiO<sub>2</sub> (101) due to lower energy of the  $E_{\text{ads}}$ . For R-TiO<sub>2</sub> (110), C2 is strongly adsorbed on the surface. For coke adsorption of C3, it has the highest adsorption energy. This suggested that C3 may be less stable during the reaction involving coke species. The stable adsorbed species are C1 > C2 > C3, respectively, on A-TiO<sub>2</sub> (101) while on R-TiO<sub>2</sub> (110) surfaces are C2 > C1 > C3, respectively.



**Figure 22** The most stable adsorption configuration of C1, C2, and C3 on A-TiO<sub>2</sub> (101) surface in GGA+U4-D3 method and R-TiO<sub>2</sub> (110) surface in GGA+U6-D3 method

## 4.2 The effect of O-vac on coke formation on TiO<sub>2</sub> catalyst

### 4.2.1 The investigation of oxygen vacancy active site on defect TiO<sub>2</sub> surfaces

We investigated the effect of O-vac on the TiO<sub>2</sub> catalyst. The possible oxygen vacancy sites have been widely reported as the most straightforward position to remove on the surface. For A-TiO<sub>2</sub> (101), The possible oxygen vacancy sites of O1, O2, and O3, while on R-TiO<sub>2</sub> (110), the possible oxygen vacancy sites of O1 and O2 as shown in Figure 23. The formation energies of O-vac on A-TiO<sub>2</sub> (101) and R-TiO<sub>2</sub> (110) surfaces without U and D3 terms were shown in Table 4.

The result indicates that O1 site has the lowest formation energy on both surfaces, as in other works [43, 53]. The O-vac formation energy of the O1 site were 4.99 and 3.37 eV for the most stable structures of O-vac on A-TiO<sub>2</sub> (101) and R-TiO<sub>2</sub> (110), respectively. Moreover, the O-vac formation energy value on the A-TiO<sub>2</sub> (101) surface was higher than that of R-TiO<sub>2</sub> (110) due to the reason for the lower density of O-vac on the A-TiO<sub>2</sub> (101) and roleplay in its higher activity compared to R-TiO<sub>2</sub> (110) surface [53].

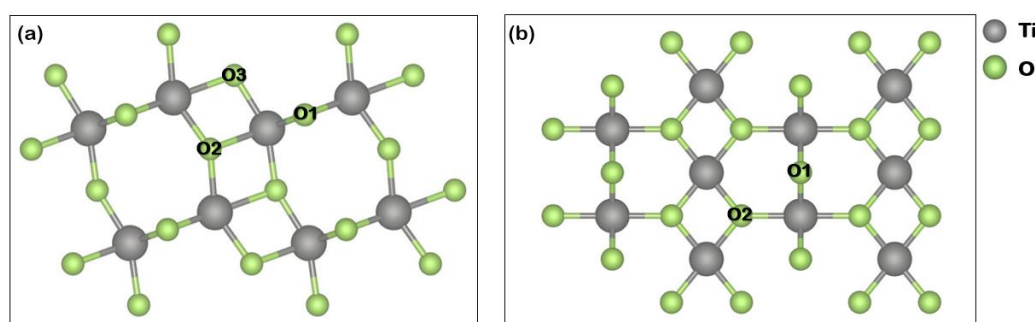


**Figure 23** The slab models in top view with the possible oxygen vacancy sites on (a) the A-TiO<sub>2</sub> (101) and (b) the R-TiO<sub>2</sub> (110) surfaces

**Table 4** Formation energies, in eV, of O-vac defects at different surface sites of A-TiO<sub>2</sub> (101) and R-TiO<sub>2</sub> (110)

Catalyst surface	Defect site	Formation energy (eV)	
		LDA	GGA
A-TiO <sub>2</sub> (101)	<b>O1</b>	<b>5.41</b>	<b>4.99</b>
	O2	6.05	5.41
	O3	5.83	5.21
R-TiO <sub>2</sub> (110)	<b>O1</b>	<b>3.85</b>	<b>3.37</b>
	O2	4.77	4.14

#### 4.2.2 Coke evolution on O-vac A-TiO<sub>2</sub> (101) and R-TiO<sub>2</sub> (110) surfaces

To understanding the interaction between cokes on O-vac A-TiO<sub>2</sub> (101) and R-TiO<sub>2</sub> (110) surfaces, each C1, C2, and C3 adsorption is also investigated in this section.

All stable configurations of C1 adsorption on A-TiO<sub>2</sub> (101) and R-TiO<sub>2</sub> (110) surfaces, which are given in Figure 24 and Figure 25, respectively. The result shows the position of O3 active site is the most attractive or stable active site on O-vac A-TiO<sub>2</sub> (101) surface while for O-vac R-TiO<sub>2</sub> (110) surface is B1 active site for adsorption that carbon should choose to adsorb as a first site (noted that B1 active site is also labeled as O1'). However, the other active sites that have lower  $E_{\text{ads}}$  cannot be chosen due to after carbon adsorbed on the catalyst surface; the catalyst surface is reconstructed as the position of the B1 and H1 active sites that the oxygen is pushed out of the O-vac A-TiO<sub>2</sub> (101) surface.

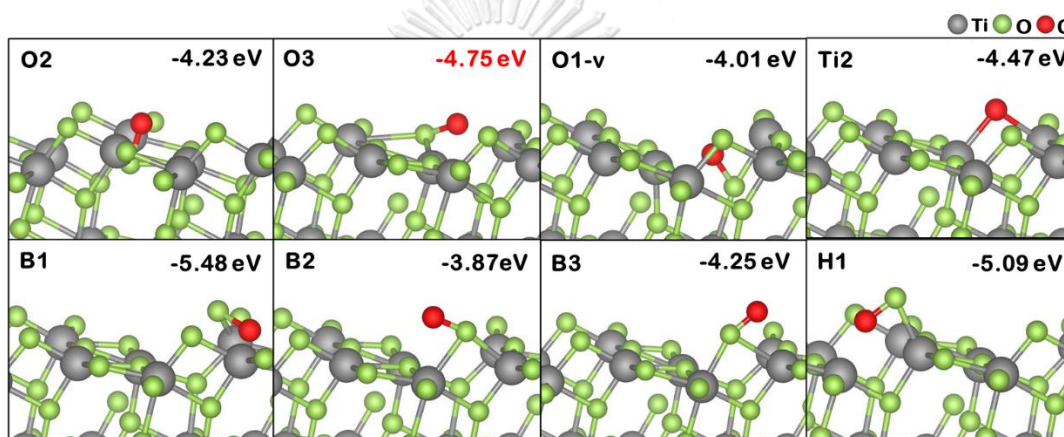


**Figure 24** All stable configurations of C1 adsorption on O-vac A-TiO<sub>2</sub> (101) surface in GGA method

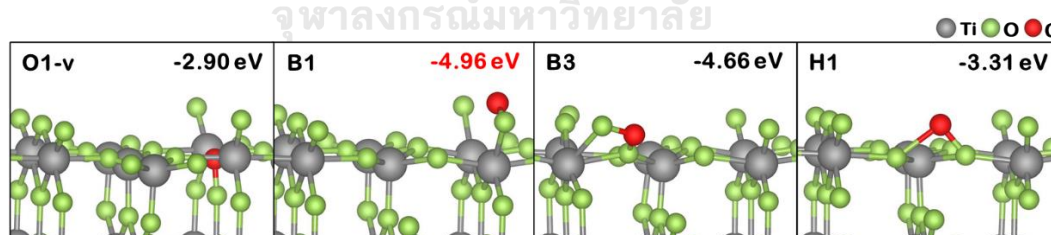


**Figure 25** All stable configurations of C1 adsorption on O-vac R-TiO<sub>2</sub> (110) surface in GGA method

We studied coke formation on O-vac A-TiO<sub>2</sub> (101) and R-TiO<sub>2</sub> (110) surfaces in GGA+U4-D3 and GGA+U6-D3 methods, respectively. For O-vac on A-TiO<sub>2</sub> (101), which are given in Figure 26, The active site of C1 adsorption changed from the O1 to O3 active site due to the O3 active site is located near the oxygen vacancy, which

induces some electrons on the two Ti atoms next to the vacancy location during oxygen deficit [53]. After the coke evolution to C2 and C3 adsorption, the active site changed from O3 to Ti1 and Ti2 sites. Interestingly, the C3 adsorbed as cyclic coke. The  $E_{\text{ads}}$  of C1, C2 and C3 adsorption are -3.76, -6.21 and -4.65 eV, respectively. The bond distance between the active site and coke adsorption can be shown in Table 5. The results reveal that C2 is strongly adsorbed on the A-TiO<sub>2</sub> (101) surface as it has the lowest value of  $E_{\text{ads}}$ .

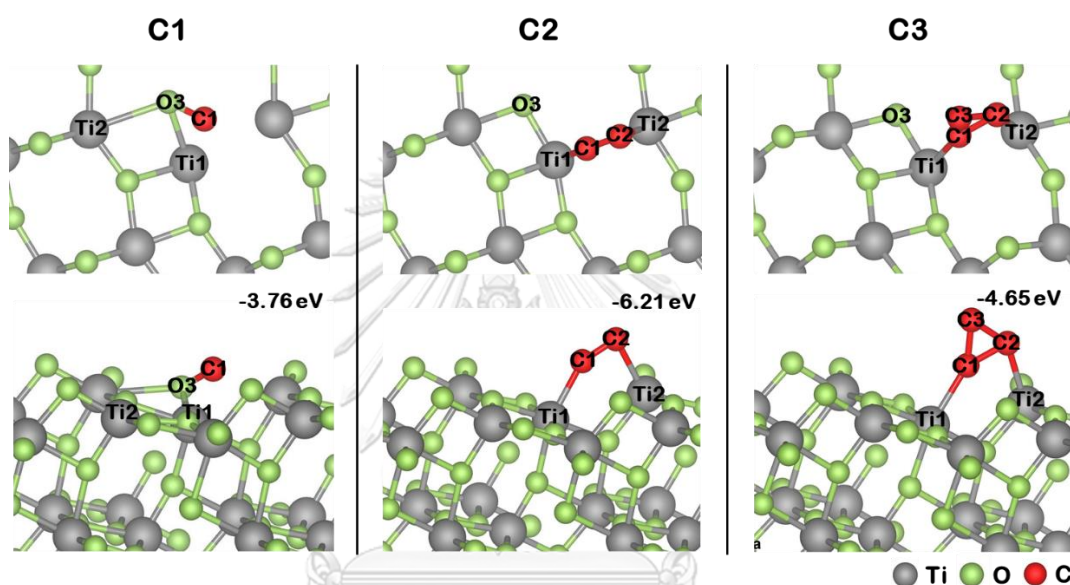


**Figure 26** The most stable adsorption configuration of C1, C2, and C3 on O-vac A-TiO<sub>2</sub> (101) surfaces in GGA+U4-D3

For O-vac on the R-TiO<sub>2</sub> (110), which is given in Figure 27. The  $E_{\text{ads}}$  of C1, C2 and C3 adsorption are -6.15 eV, -5.34 eV and -4.15 eV, respectively. The bond distance between the active site and coke adsorption can be shown in Table 5. The active site of C1 adsorption is found to consume the O1' active site on the R-TiO<sub>2</sub> (110) surface, forming a carbon monoxide (CO) molecule that desorbed after the process. The C1-O1' bond length is 1.18 Å [54]. However, this CO formation may generate a new oxygen vacancy. After the coke evolution to C2, the active site changed from O1' to Ti1 site due to the oxygen vacancy near O1' active site, which induces some electrons on the two Ti atoms next to the vacancy location during oxygen deficit. Interestingly, the coke evolution of C3, the C3 atom interacts with the O1' active site.

The results reveal that the C2 is strongly adsorbed on the O-vac R-TiO<sub>2</sub> (110) surface, not included the C1 due to the reconstruction of the O-vac R-TiO<sub>2</sub> (110) surface.

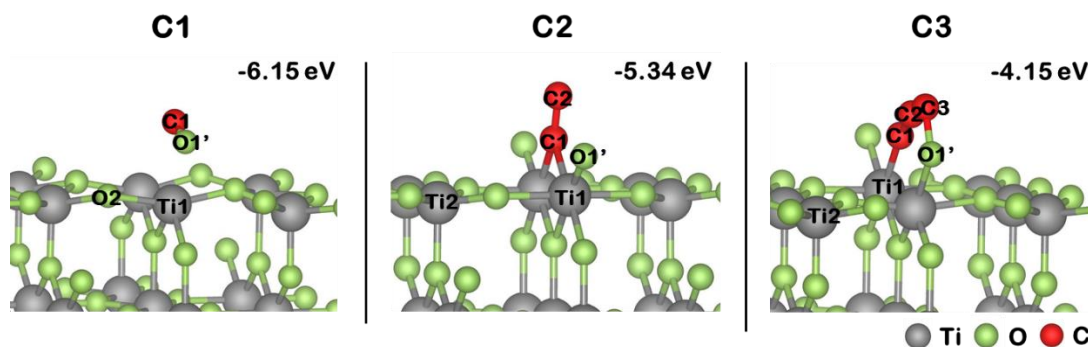


**Figure 27** The most stable adsorption configuration of C1, C2, and C3 on R-TiO<sub>2</sub> (110) surfaces in GGA+U6-D3

**Table 5** The bond distance (*d*) between active site and Coke adsorption on A-TiO<sub>2</sub> (101) and R-TiO<sub>2</sub> (110) surfaces

surface	absorbate	<i>d</i> (Å)
A-TiO <sub>2</sub> (101)	C1	$d_{O3-C1} = 2.06$
	C2	$d_{Ti1-C1} = 2.09$ $d_{Ti2-C2} = 2.06$
	C3	$d_{Ti1-C1} = 2.14$ $d_{Ti2-C2} = 2.07$
R-TiO <sub>2</sub> (110)	C1	$d_{O1'-C1} = 1.18$
	C2	$d_{Ti1-C1} = 2.10$
	C3	$d_{O1'-C3} = 1.33$ $d_{Ti1-C1} = 2.20$

### 4.3 Electronic properties of coke on perfect and O-vac TiO<sub>2</sub> surfaces

#### 4.3.1 Bader charge and charge density difference analysis

The insight information of electron depletion and accumulation during the coke adsorption on the A-TiO<sub>2</sub> (101) surface was determined based on the Bader charge and charge density difference analysis demonstrated by yellow and pink regions,

respectively, as shown in Figure 28. The number of valence electrons of a neutral atom is used as a reference for this calculation. The positive and negative signs represent the losing and gaining of the electrons at the U value of 4 eV with D3 correction. The large amount of electron transfer from the adsorbed C1 (denoted as +0.78 |e|) to A-TiO<sub>2</sub> (101) surface (denoted as -0.78 |e|) indicates electron transfer from C1 coke to A-TiO<sub>2</sub> (101) surface. The adsorbed C1 interacts with the O1 active site as observed by the electron depletion of C1, which links to the electron accumulation around the Ti1 atom. When C2 adsorbed, it was indicated that electron transfer from C2 coke to A-TiO<sub>2</sub> (101) surface. The C1 of adsorbed C2 interacts with O1 active site as observed by the electron depletion (denoted as +0.30 |e|) and the C2 interacts with C1 as observed by electron accumulation (denoted as -0.21 |e|). The C1 and C2 atoms of adsorbed C3 that interacts with O1 and C1 active site, respectively, as observed by the electron depletion (denoted as +0.12 |e| and +0.11 |e|, respectively) while the C3 that interacts with C2 as observed by electron accumulation (denoted as -0.21 |e|).

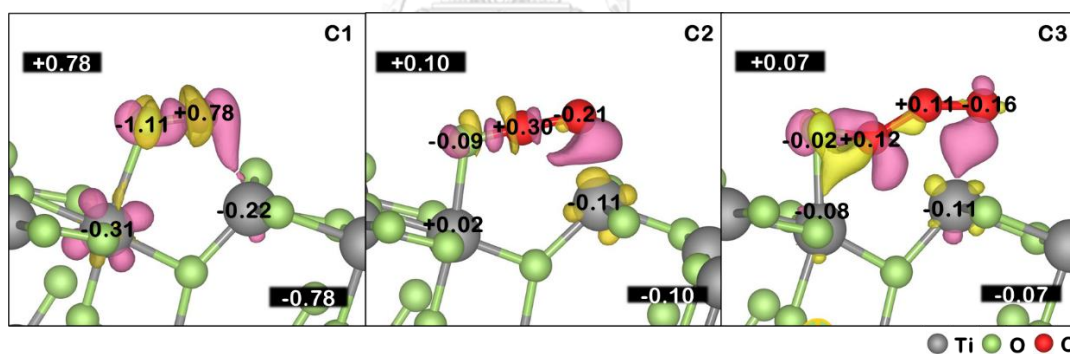


**Figure 28** The charge density difference of C1, C2 and C3 adsorption on A-TiO<sub>2</sub> (101) in GGA+U4-D3 method are shown in yellow and pink regions as electron depletion and electron accumulation, respectively. The electron gain (-) and loss (+) with an isovalue of  $\pm 0.017$  |e|/Å

The insight information of electron depletion and accumulation during the coke adsorption on the R-TiO<sub>2</sub> (110) surface at the U value of 6 eV with D3 correction was determined based on the Bader charge analysis and demonstrated by yellow and pink regions, respectively, as shown in Figure 29. The C1 adsorbed by creating two

bonds with the surface oxygen of the catalyst: C1-O1 and C1-O2. Moreover, the adsorbed C1 also interacts with the Ti2 active site as observed by the electron depletion of C1, which links to the electron accumulation around the Ti2 atom. Besides, a large amount of electron transfer from the adsorbed C1 (denoted as +0.86 |e|) to R-TiO<sub>2</sub> (110) surface (denoted as -0.86 |e|) also confirms a strong interaction of C1 to the R-TiO<sub>2</sub> (110) surface and the electron transfer on the surface at Ti2 active site, the charge disperses to another Ti2 active site near O2 site (denoted as -0.29 |e|). The Bader charge change between C2 evolution (denoted as +0.07 |e|) and the R-TiO<sub>2</sub> (110) surface (denoted as -0.07 |e|) while between C3 evolution (denoted as +0.49 |e|) and the R-TiO<sub>2</sub> (110) surface (denoted as -0.49 |e|), these indicate electron transfer from coke evolution of C2 and C3 to R-TiO<sub>2</sub> (110) surface. In the case of higher coke, the C3 species exhibited a similar trend in the increment of electron exchange between the C3 and R-TiO<sub>2</sub> (110) surface.

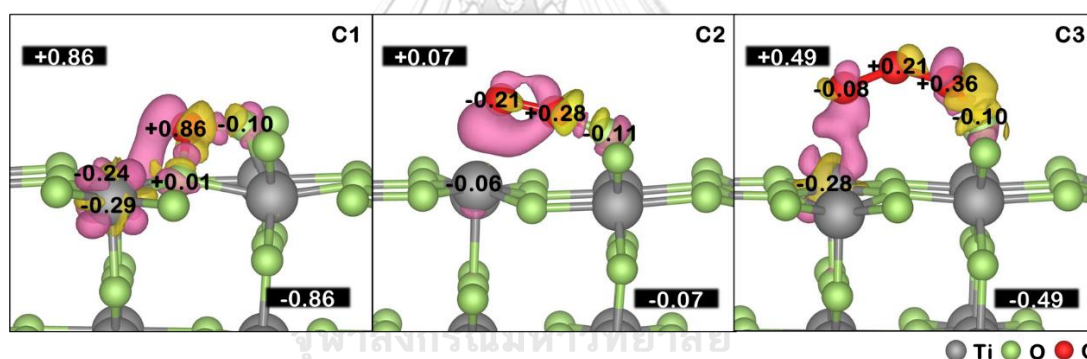


**Figure 29** The charge density difference of C1, C2 and C3 adsorption on R-TiO<sub>2</sub> (110) in GGA+U6-D3 method are shown in yellow and pink regions as electron depletion and electron accumulation, respectively. The electron gain (-) and loss (+) with an isovalue of  $\pm 0.017$  |e|/Å

The analysis of their electronic properties was determined by the Bader charge analysis and charge density difference, as shown in Figure 30. On O-vac the A-TiO<sub>2</sub> (101) surface, it was indicated that the behavior of electron transfer from O-vac A-TiO<sub>2</sub> (101) surface (denoted as +0.14 |e|) to C1 coke (denoted as -0.14 |e|) as observed by electron accumulation. When C2 adsorbed on O-vac A-TiO<sub>2</sub> (101)

surface, it was indicated that electron transfer from O-vac A-TiO<sub>2</sub> (101) surface (denoted as +1.05 |e|) to C2 coke (denoted as -1.05 |e|). The C1 of adsorbed C2 interacts with Ti1 active site as observed by the electron accumulation (denoted as -0.44 |e|) and the C2 that interacts with C1 as observed by electron accumulation (denoted as -0.17 |e|). The C1 and C2 atoms of adsorbed C3 that interacts with Ti1 and Ti2 active sites, respectively, as observed by the electron accumulation (denoted as -0.52 |e| and -0.43 |e|, respectively) also the C3 that interacts with C1 and C2 as observed by electron accumulation (denoted as -0.004 |e|).

For O-vac R-TiO<sub>2</sub> (110) surface, electron transfer from C1 coke (denoted as +0.87 |e|) to O-vac R-TiO<sub>2</sub> (110) surface (denoted as -0.87 |e|) as observed by electron depletion. The Bader charge change between C2 evolution (denoted as -1.09 |e|) and the O-vac R-TiO<sub>2</sub> (110) surface (denoted as +1.09 |e|) while between C3 evolution (denoted as -0.16 |e|) and the O-vac R-TiO<sub>2</sub> (110) surface (denoted as +0.16 |e|), these indicate that when the surface has the oxygen deficiency, the electron transfer from both O-vac A-TiO<sub>2</sub> (101) and R-TiO<sub>2</sub> (110) surface to coke formation of C2 and C3 as the electron accumulation.

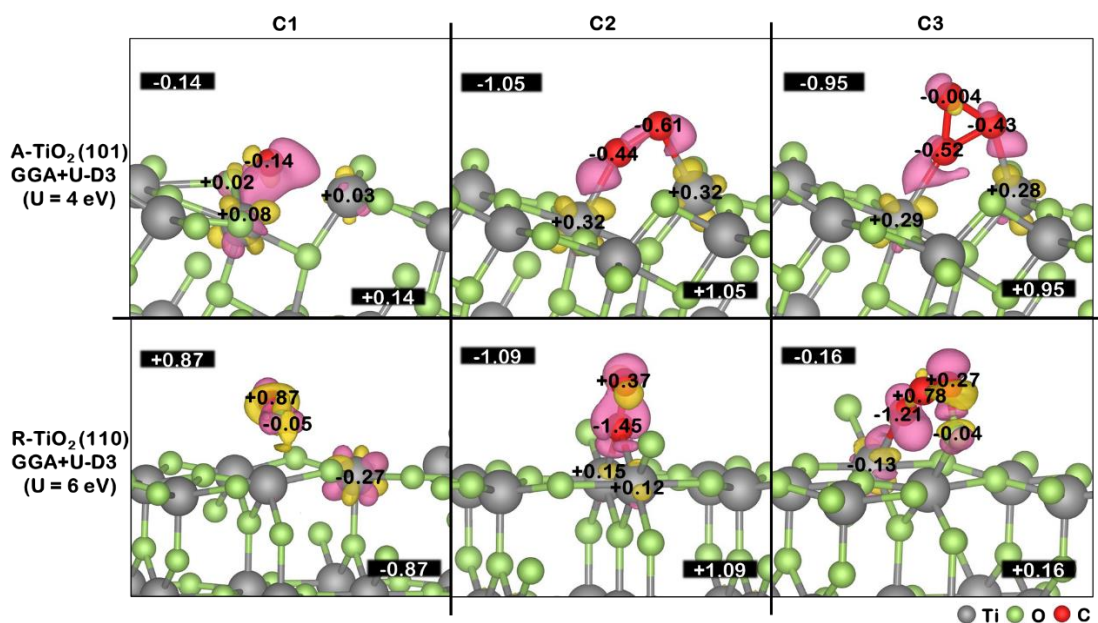


**Figure 30** The charge density difference of C1, C2 and C3 adsorption on O-vac of A-TiO<sub>2</sub> (101) and R-TiO<sub>2</sub> (110) surfaces are shown in yellow and pink regions as electron depletion and electron accumulation, respectively. The electron gain (-) and loss (+) with an isovalue of  $\pm 0.017 |e|/\text{\AA}$

#### 4.3.2 Projected density of states (PDOS) analysis

The projected density of states (PDOS) was examined to describe the energy of states occupied in the surface systems of coke evolution on perfect and defect A-TiO<sub>2</sub> (101) and R-TiO<sub>2</sub> (110) surfaces. The effect of the Hubbard U correction at the appropriate U value of each catalyst surface and D3 dispersion representing the repulsion of electrons in the systems is also studied.

The negative and positive zone represent the valence and conduction states, respectively. The plots of the projected density of state (PDOS) of perfect A-TiO<sub>2</sub> (101) and R-TiO<sub>2</sub> (110) surfaces under different methods are expressed, as shown in Figure 31. For the A-TiO<sub>2</sub> (101), the PDOS profile of the valence state is located around  $-4.25$  eV to  $-0.04$  eV for GGA method. For GGA+U4 and GGA+U4-D3 methods, the valence state is located around  $-4.21$  eV to  $-0.01$  eV and  $-4.25$  eV to  $-0.02$  eV, respectively. Moreover, the PDOS profile of the conduction state is observed in the range of  $2.75$  eV to  $6.40$  eV for the GGA method. For GGA+U4 and GGA+U4-D3

methods, the conduction state is observed in the range of 3.28 eV to 6.36 eV and 3.27 eV to 6.35 eV. The energy gap ( $E_g$ ) is 2.79 eV, 3.29 eV, and 3.29 eV, respectively for GGA, GGA+U4, and GGA+U4-D3 methods. For the R-TiO<sub>2</sub> (110), the PDOS profile of the valence state is located around -6.23 eV to -0.04 eV for the GGA method. For GGA+U6 and GGA+U6-D3 methods, the valence state is around -6.36 eV to -0.01 eV and -6.37 eV to -0.01 eV, respectively. Moreover, the PDOS profile of the conduction state is observed in the range of 0.96 eV to 5.44 eV for the GGA method. For GGA+U6 and GGA+U6-D3 methods, the conduction state is observed in the range of 1.53 eV to 5.34 eV and 1.53 eV to 5.37 eV. The energy gap ( $E_g$ ) is 1.01 eV, 1.54 eV, and 1.54 eV, respectively for GGA, GGA+U6, and GGA+U6-D3 methods.

The results indicated that the addition of U term with/without D3 correction shifted the conduction state from the valence state and narrowed the conduction state due to the increase in electron repulsion that localized in the d-orbital. The  $E_g$  of perfect A-TiO<sub>2</sub> (101) surface with the addition of U (4 eV) is 3.29 eV, which makes the  $E_g$  close to the experiment value (3.21 eV [14, 55]). Although the  $E_g$  of R-TiO<sub>2</sub> (110) surface with the addition of U (6 eV) cannot adjust the  $E_g$  of the rutile close to the experiment (3.00 eV [55]), even though the U value is higher than 7 eV to correct the  $E_g$ , it will elongate the Ti-O bond distances as M. E. Arroyo-de Dompablo *et al.* revealed that the large U values lead to a poor interatomic distances [15]. Therefore, the U at 6 eV can be chosen for the model on the R-TiO<sub>2</sub> (110) surface because it still gives the Ti-O bond distances around 1.96 Å close to the experiment value (1.94 – 1.97 Å [56]).

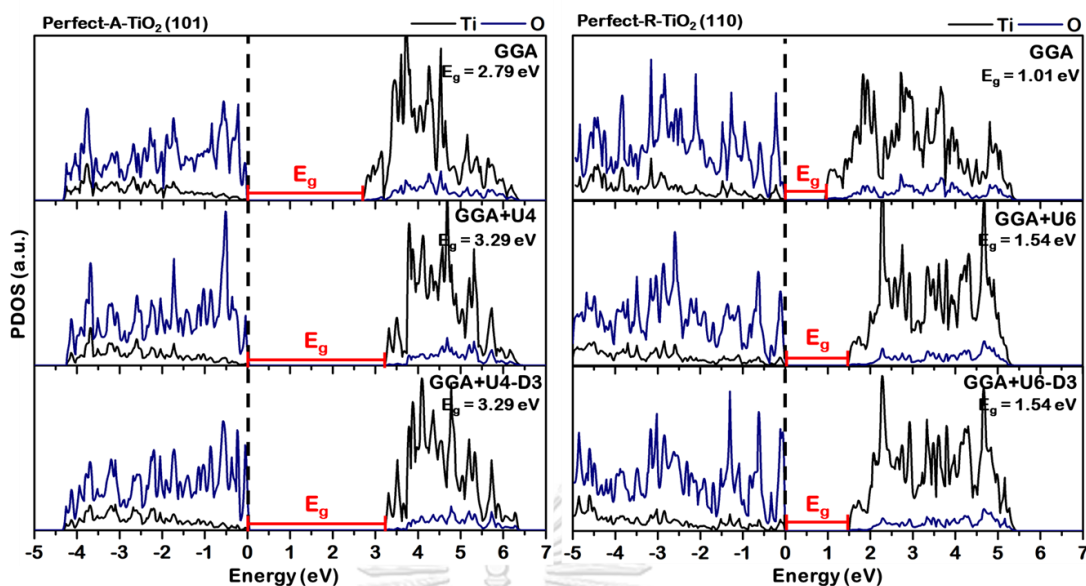


**Figure 31** The projected density of state (PDOS) of perfect A-TiO<sub>2</sub> (101) and R-TiO<sub>2</sub> (110) surfaces in various methods

For C1, C2, and C3 adsorption on A-TiO<sub>2</sub> (101) and O-vac A-TiO<sub>2</sub> (101) surface in the GGA+U4-D3 method are given in Figure 32. After C1 adsorption on the A-TiO<sub>2</sub> (101) surface, the C states has been detected in the conduction band, suggests that carbon atomic also interacts with the Ti2 site. When C2 adsorbed on A-TiO<sub>2</sub> (101) surface, the C peak was found around -0.05 eV to -0.01 eV that is also composed of 2p orbitals of O atoms, which reveals the bonding of C and O atom. After the C3 adsorption, the C states has been detected at the top of the valence band and the bottom of the conduction band. The result suggests the C atoms interact with both O1 and Ti2 sites, which relate to the result of the charge density difference in Figure 28.

For C1, C2 and C3 adsorption on O-vac A-TiO<sub>2</sub> (101) surface occurs the unpaired electronic states of oxygen vacancy were detected between -0.01 eV and -0.89 eV, comprised mainly of the Ti-state for C1 and C3 adsorption, while for C2 adsorption comprised of the O-state. The C peaks were detected, which indicated the electron from the O-vac A-TiO<sub>2</sub> (101) transfer to cokes. These peaks correlated with the charge accumulation region as pink regions confirmed via the Bader charge analysis, illustrated in Figure 30.

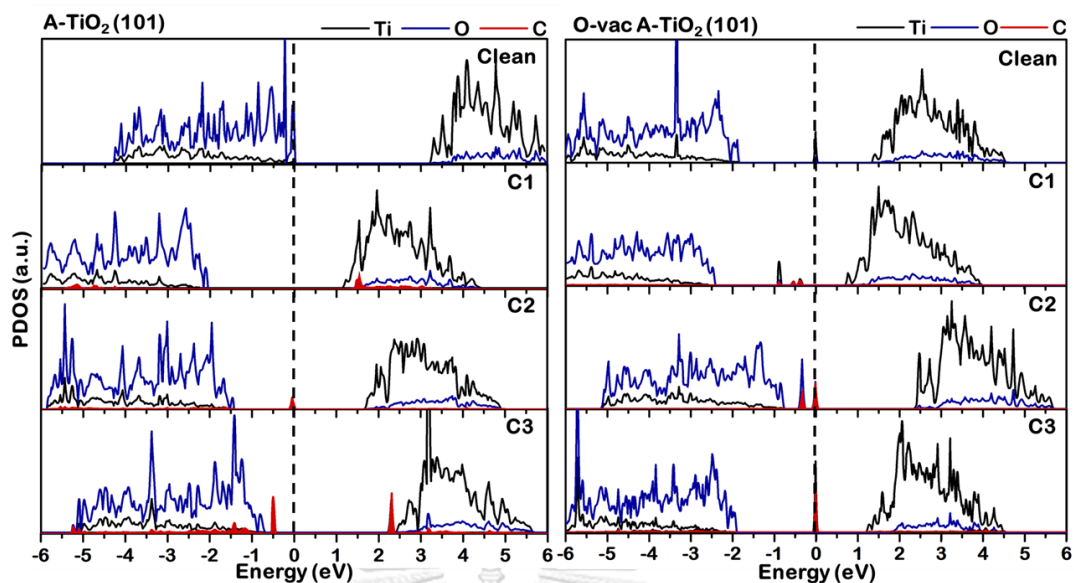


**Figure 32** The projected density of state (PDOS) of C1, C2, and C3 adsorption on A-TiO<sub>2</sub> (101) and O-vac A-TiO<sub>2</sub> (110) in GGA+U4-D3 method

For C1, C2, and C3 adsorption on R-TiO<sub>2</sub> (110) and O-vac R-TiO<sub>2</sub> (110) surfaces in the GGA+U6-D3 method, the projected density of state (PDOS) was analyzed as shown in Figure 33. The results show that after C1 adsorption on R-TiO<sub>2</sub> (110) surface, the C peak has been detected between  $-0.01$  eV and  $-0.13$  eV, which comprised mainly of the Ti-state. When C2 adsorbed on the R-TiO<sub>2</sub> (110) surface, the C states were detected at the top of the valence band suggest the composition of 2p orbitals of O atoms, which reveals the bonding of C and O atom. However, the PDOS of C2 adsorption shifted, which indicated that the surface acts as electron depletion and implied changes in reactivity as a catalyst, even from Bader charge analysis has small negative value. As a result, only the Bader charge analysis might not be able to determine the electronic properties. After the C3 adsorption, the C states has been detected at the top of the valence band and the bottom of the conduction band. The result suggests the C atoms interact to both O1 and Ti2 sites. These peaks related to the charge depletion region confirmed by the Bader charge analysis illustrated in Figure 29.

For C1 adsorption on O-vac R-TiO<sub>2</sub> (110) surface occurs the unpaired electronic states of oxygen vacancy and the C peak was detected between  $-0.17$  eV and  $0.07$

eV, comprised mainly of the Ti-state. However, no sign of CO molecule was detected. For C2 adsorption, the unpaired electronic states of oxygen vacancy were detected at -0.94 eV, comprised of the O-state and the C peaks were detected between -0.94 eV and -1.27 eV. For C3 adsorption, the unpaired electronic states of oxygen vacancy were found between -0.39 eV and 0.20 eV, comprised mainly of the Ti-state and the C peak was found at -0.39 eV. These results correlated to the Bader charge analysis, illustrated in Figure 30, indicated when C2 and C3 adsorbed on the surface, the electron from the O-vac R-TiO<sub>2</sub> (110) transfer to cokes while for C1 adsorbed, the electron transfer from atomic coke to O-vac R-TiO<sub>2</sub> (110) surface.

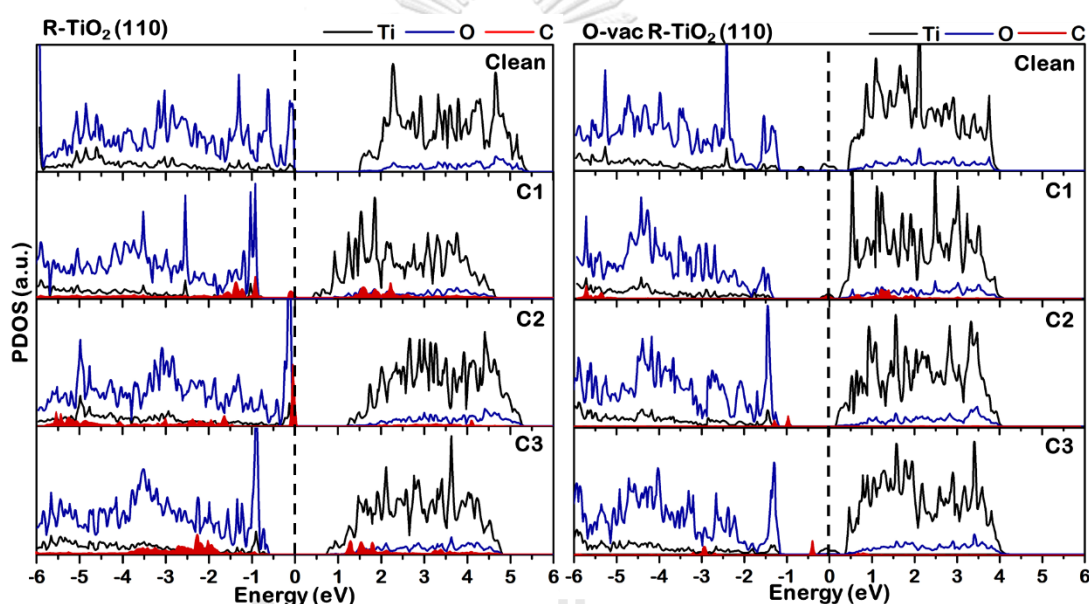


**Figure 33** The projected density of state (PDOS) of C1, C2, and C3 adsorption on R-TiO<sub>2</sub> (110) and O-vac R-TiO<sub>2</sub> (110) in GGA+U6-D3 method

To investigate the effect of O-vac on coke adsorption from PDOS profiles for O-vac A-TiO<sub>2</sub> (101) surface, The results indicate that electron transfer from carbon to O-vac A-TiO<sub>2</sub> (101) surface during the coke formation process. For O-vac R-TiO<sub>2</sub> (110), the occurrence of the unpaired electronic states of oxygen vacancy shifted the conduction states close to the Fermi level refers the electrons from the valence band will be easier to travel to the conduction band increasing the reactivity of the materials and become more reactive catalysts [57].

#### 4.4 The effect of temperature on coke formation on TiO<sub>2</sub> surfaces

This section describes the effect of temperature during coke adsorption on both A-TiO<sub>2</sub> (110) and R-TiO<sub>2</sub> (110) surfaces is described. To investigate the effect of temperature in the range of 400-1000°C, the  $\Delta G_{\text{ads}}$  of coke adsorption on A-TiO<sub>2</sub> (101) and O-vac A-TiO<sub>2</sub> (101) surfaces at different temperatures (°C) is plotted in Figure 34. The solid and dash lines represent the coke adsorption on perfect and defect surfaces, respectively. As a result of the increased temperature, the  $\Delta G_{\text{ads}}$  have a lower negative value, indicating a weaker interaction between cokes and catalyst surfaces. For coke adsorption on the A-TiO<sub>2</sub> (101) surface, the C1 adsorption has the most negative value of  $\Delta G_{\text{ads}}$  while the C2 adsorption has the most negative value of  $\Delta G_{\text{ads}}$  for O-vac A-TiO<sub>2</sub> (101). These results correlated to Bader charge analysis that shows a large amount of electrons on the catalyst surface.

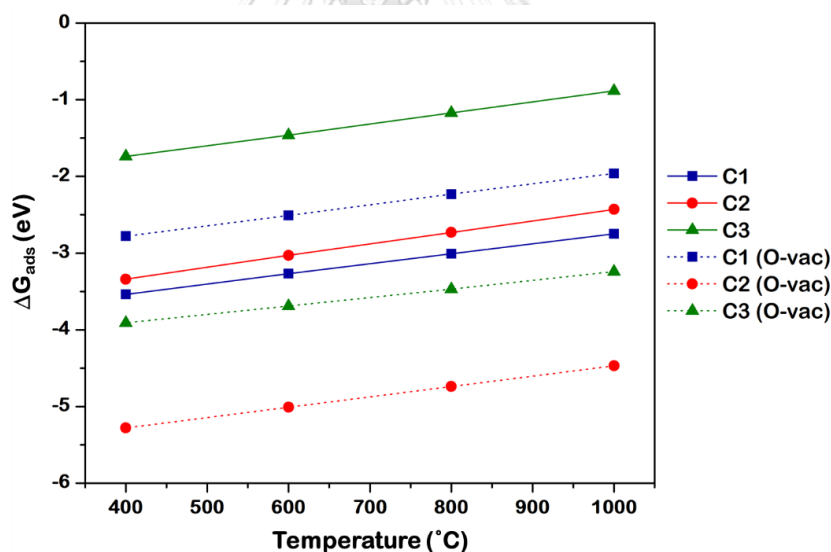


**Figure 34** The Gibbs free energy changes ( $\Delta G_{\text{ads}}$ ) of coke adsorption on A-TiO<sub>2</sub> (101) and O-vac A-TiO<sub>2</sub> (101) surfaces in Different temperature (°C)

The  $\Delta G_{\text{ads}}$  of coke adsorption on R-TiO<sub>2</sub> (110) and O-vac R-TiO<sub>2</sub> (110) surfaces at different temperatures (°C) is plotted in Figure 35. The results also exhibit a similar trend of the  $\Delta G_{\text{ads}}$  when the temperature is increased as coke adsorption on anatase surface. For coke adsorption on R-TiO<sub>2</sub> (110) surface, the C2 adsorption has the most

negative value of  $\Delta G_{\text{ads}}$ , which correlated to PDOS analysis that of C2 adsorption shifted which indicated that surface act as electron depletion. For coke adsorption on O-vac R-TiO<sub>2</sub> (110) surface, the C1 adsorption has the most negative value of  $\Delta G_{\text{ads}}$ , which can be caused by the CO formation that might generate a new oxygen vacancy site.

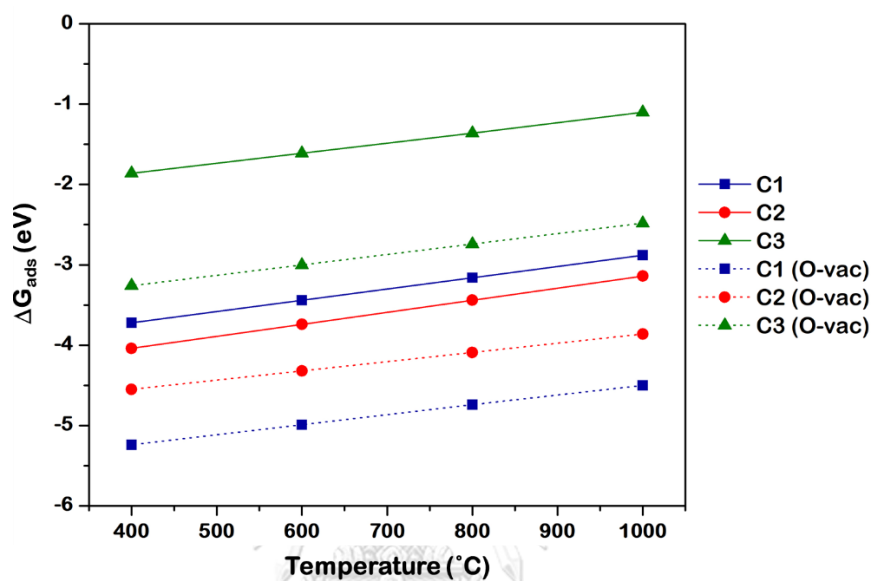


**Figure 35** The Gibbs free energy changes ( $\Delta G_{\text{ads}}$ ) of coke adsorption on R-TiO<sub>2</sub> (110) and O-vac R-TiO<sub>2</sub> (110) surfaces in Different temperature (°C)

## CHAPTER V

### Conclusion

This work explores coke formation on the perfect and defected  $\text{TiO}_2$ . The effects of Hubbard U correction and the incorporation of the Van der Waal term on the accuracy of the electronic properties and adsorption energy were investigated. The results showed that the GGA method is more suitable than the LDA method due to the gradient of non-uniformity electron density, which gives a better accuracy result. The presence of the Hubbard U correction provides a more accurate quantitative of the result. The appropriate U value of A- $\text{TiO}_2$  (101) is 4 eV because the structure has a small change and no breaking bond, while the appropriate U value of R- $\text{TiO}_2$  (110) is 6 eV. The Van der Waal correction contributes to the improvement of adsorption, promoting more negative adsorption energy. However, the bond length of Ti-O bonds on  $\text{TiO}_2$  surfaces is elongated. For the coke formation on A- $\text{TiO}_2$  (101) and R- $\text{TiO}_2$  (110), the electron transfer from coke to surface. The stability adsorbed species are in orders:  $C1 > C2 > C3$  on A- $\text{TiO}_2$  (101) surface, and  $C2 > C1 > C3$  on R- $\text{TiO}_2$  (110) surface. For the effect of oxygen vacancy on coke formation, the results reveal that C2 is strongly adsorbed on O-vac A- $\text{TiO}_2$  (101) and O-vac R- $\text{TiO}_2$  (110) surfaces. Moreover, when the coke evolved from C1 to C2 and C3, the active site changed from O to Ti active site and the electron transfer from catalyst surface to coke. This can be suggested that the defect surface is more active than the perfect surface, which may lead to higher stability of coke deposition. For the effect of temperature in the range of 400-1000°C when the temperature increases, the interaction between cokes and catalyst surfaces becomes weaker adsorption strength. Comparing between coke formation on A- $\text{TiO}_2$  (101) and R- $\text{TiO}_2$  (110) surfaces, interaction between coke and R- $\text{TiO}_2$  (110) surface is stronger than A- $\text{TiO}_2$  (101) surface. It is suggested that the coke formation on the R- $\text{TiO}_2$  (110) surface is more severe than on the A- $\text{TiO}_2$  (101) surface. Thus, prohibiting the phase transformation during the reaction is key to a high-performance  $\text{TiO}_2$  catalyst for a thermocatalytic process.



APPENDICES

จุฬาลงกรณ์มหาวิทยาลัย  
**CHULALONGKORN UNIVERSITY**

## APPENDIX A

### CALCULATION FOR ADSORPTION ENERGY

The adsorption energy ( $E_{\text{ads}}$ ) follows the equation below:

$$E_{\text{ads}} \text{ (eV)} = E_{\text{C}_n/\text{surface}} - (E_{\text{C}_n} + E_{\text{surface}}) \quad (\text{A1})$$

where  $E_{\text{C}_n/\text{surface}}$  is the total energy of the adsorption of Carbon n atom on catalyst surfaces,  $E_{\text{C}_n}$  is the total energy of isolate coke n atom in a vacuum, and  $E_{\text{surface}}$  is the total energy of the surface, respectively.

For example, the model of C1 adsorption on A-TiO<sub>2</sub> (101) surface with the total energy is illustrated as shown in Figure A1.

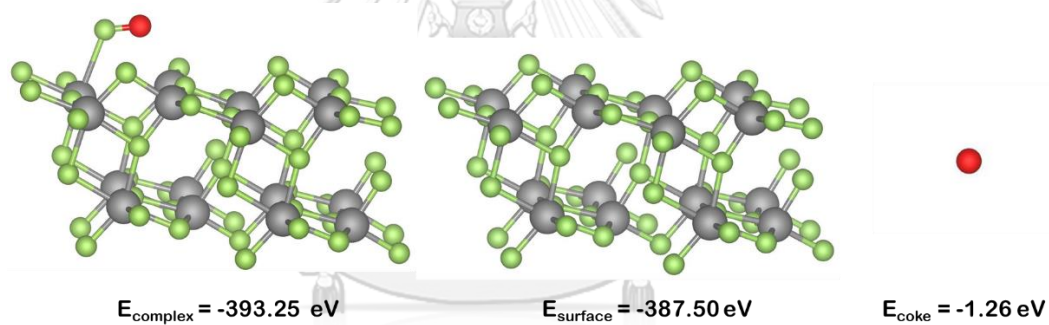


**Figure A1** The model of C1 adsorption on A-TiO<sub>2</sub> (101) surface with the total energy

$$\begin{aligned}
 E_{\text{ads}} \text{ (eV)} &= E_{\text{C}_1/\text{surface}} - (E_{\text{C}_1} + E_{\text{surface}}) \\
 &= -393.25 - ((-1.26) + (-387.50)) \\
 &= -4.49 \text{ eV}
 \end{aligned}$$

## APPENDIX B

## CALCULATION FOR FORMATION ENERGY

The formation energy was determined from the equation:

$$E_{\text{form}} \text{ (eV)} = E_{\text{O-vac}} - E_{\text{perfect}} + \frac{1}{2} E_{\text{O}_2} \quad (\text{A2})$$

where  $E_{\text{O}_2}$  is the total energy of  $\text{O}_2$  molecules (eV),  $E_{\text{O-vac}}$  is the total energy of the surface with oxygen vacancy (eV), and  $E_{\text{perfect}}$  is the total energy of the surface without oxygen vacancy (eV)

For the formation energy of O-vac A-TiO<sub>2</sub> (101) surface in GGA method at O1, O2, and O3 active sites on surface can be calculate as equation below

$$E_{\text{from,O1}} = (-417.38) - (-427.31) + (-4.94) = 4.99 \text{ eV}$$

$$E_{\text{from,O2}} = (-416.96) - (-427.31) + (-4.94) = 5.42 \text{ eV}$$

$$E_{\text{from,O3}} = (-417.16) - (-427.31) + (-4.94) = 5.21 \text{ eV}$$

For the formation energy of O-vac R-TiO<sub>2</sub> (110) surface in GGA method at O1 and O2 active sites on surface can be calculate as equation below

$$E_{\text{from,O1}} = (-625.98) - (-634.28) + (-4.94) = 3.37 \text{ eV}$$

$$E_{\text{from,O2}} = (-625.20) - (-634.28) + (-4.94) = 4.14 \text{ eV}$$

## APPENDIX C

## CALCULATION FOR GIBBS FREE ENERGY

For example, Gibbs free energy of carbon adsorption on A-TiO<sub>2</sub> (101) surface at 400°C (673 K)

**Table C1** Vibrational frequency of carbon adsorption on A-TiO<sub>2</sub> (101) surface at 673 K

C1 (Ads)			
$\omega$ (cm <sup>-1</sup> )	$\omega$ (s <sup>-1</sup> )	qvib	ZPE (eV)
1357.330752	4.07×10 <sup>13</sup>	1.06	0.0842
277.785618	8.33 ×10 <sup>12</sup>	2.23	0.0172
197.86832	5.94 ×10 <sup>12</sup>	2.90	0.0123
C2 (Ads)			
$\omega$ (cm <sup>-1</sup> )	$\omega$ (s <sup>-1</sup> )	qvib	ZPE (eV)
1927.6063	5.78E+13	1.02E+00	0.1196
771.91323	2.32E+13	1.24E+00	0.0479
620.9045	1.86E+13	1.36E+00	0.0385
488.49522	1.47E+13	1.54E+00	0.0303
470.46304	1.41E+13	1.58E+00	0.0292
187.12568	5.61E+12	3.03E+00	0.0116
C3 (Ads)			
$\omega$ (cm <sup>-1</sup> )	$\omega$ (s <sup>-1</sup> )	qvib	ZPE (eV)
1850.357225	5.55E+13	1.02E+00	0.1148
1436.566063	4.31E+13	1.05E+00	0.0891
819.687429	2.46E+13	1.21E+00	0.0508
483.298876	1.45E+13	1.55E+00	0.0300
458.182288	1.37E+13	1.60E+00	0.0284
397.180421	1.19E+13	1.75E+00	0.0246
296.73465	8.90E+12	2.13E+00	0.0184
197.358948	5.92E+12	2.90E+00	0.0122
142.436169	4.27E+12	3.81E+00	0.0088

1. Convert the vibrational frequency ( $\omega$ ) unit from  $\text{cm}^{-1}$  to  $\text{s}^{-1}$  following equation

$$\omega(\text{s}^{-1}) = \omega(\text{cm}^{-1}) \times c(\text{cm/s}) \quad (\text{C1})$$

where  $c$  is the speed of light equal to  $3 \times 10^{10}$   $\text{cm/s}$

2. Calculate the  $q_{\text{vib}}$  following equation

$$q_{\text{vib}} = \frac{1}{(1 - e^{(-h\omega/K_{\text{B}}T)})} \quad (\text{C2})$$

where Planck's constant ( $h$ ) is  $4.14 \times 10^{-15}$   $\text{eV s}^{-1}$ , the Boltzmann constant ( $K_{\text{B}}$ ) is  $8.617 \times 10^{-5}$   $\text{eV K}^{-1}$ , vibrational frequency ( $\omega$ ,  $\text{s}^{-1}$ ), and the temperature ( $T$ ) in kelvin

3. Calculate the total vibrational partition function ( $Q_{\text{vib}}$ ) following equation

$$Q_{\text{vib}} = \prod_1^n q_{\text{vib}_i} \quad (\text{C3})$$

where the total vibrational partition function ( $Q_{\text{vib}}$ ) of the adsorbed system in the measurement from vibrational analysis

4. Calculate the zero-point energy (ZPE) following equation

$$\text{ZPE} = \sum \frac{h\nu_i}{2} \quad (\text{C4})$$

where  $E_{\text{ZPE}}$  is the zero-point energy of the adsorbed system

5. Gibbs free energy ( $G$ ) of carbon adsorption were calculated by

$$G_i = E_i + \text{ZPE}_i - RT \ln Q_{\text{vib}} \quad (\text{C5})$$

where  $E_i$  is the total energy of species  $i$  provided from a normal DFT calculation,  $E_{\text{ZPE}}$  is the zero-point energy of adsorbed system, the gas constant ( $R$ ) is  $8.62 \times 10^{-5}$   $\text{eV K}^{-1}$ , and  $Q_{\text{vib}}$  is the total vibrational partition function of adsorbed system in which the

measurement from vibrational analysis, the results from the above in Table C1 was using to calculate the  $Q_{vib}$  and  $G_i$  are shown in Table C2.

**Table C2**  $Q_{vib}$  and  $E_{ZPE}$  of Carbon adsorption on A-TiO<sub>2</sub> (101) surface at 673 K

Adsorbed system	$Q_{vib}$	ZPE (eV)	E (eV)	E+ZPE (eV)	G (eV)
C1 (gas)	1.25E+07	0.00E+00	-1.26E+00	-1.26E+00	-2.21E+00
surface	0.00E+00	0.00E+00	-3.87E+02	-3.87E+02	-3.87E+02
C1 (ads)	6.84E+00	1.14E-01	-3.93E+02	-3.93E+02	-3.93E+02
C2 (gas)	6.46E+07	1.14E-01	-9.66E+00	-9.55E+00	-1.06E+01
surface	0.00E+00	0.00E+00	-3.87E+02	-3.87E+02	-3.87E+02
C2 (ads)	1.26E+01	2.77E-01	-4.02E+02	-4.01E+02	-4.01E+02
C3 (gas)	2.06E+08	2.21E-01	-1.90E+01	-1.88E+01	-1.99E+01
surface	0.00E+00	0.00E+00	-3.87E+02	-3.87E+02	-3.87E+02
C3 (ads)	1.32E+02	3.77E-01	-4.09E+02	-4.09E+02	-4.09E+02

6. Calculate the zero-point energy ( $\Delta E_{ZPE}$ ) of adsorbed system following equation

$$\Delta E_{ZPE} = [ E + ZPE (C_i \text{ (ads)}) ] - [ E + ZPE (\text{surface}) ] - [ E + ZPE (C_i \text{ (gas)}) ] \quad (C6)$$

where  $E_i$  is the total energy of species  $i$  provided from a normal DFT calculation,  $E_{ZPE}$  is the zero-point energy of the adsorbed system

7. Gibbs free energy changes ( $\Delta G$ ) of carbon adsorption were calculated by

$$\Delta G_{ads} = G (C_i \text{ (ads)}) - G (\text{surface}) - G (C_i \text{ (gas)}) \quad (C7)$$

where  $G (C_i \text{ (ads)})$  is the Gibbs free energy of carbon adsorbed species  $i$ ,  $G (\text{surface})$  is the Gibbs free energy of surface before carbon adsorption, and  $G (C_i \text{ (gas)})$  is the Gibbs free energy of isolate carbon species  $i$

For example,  $\Delta G$  of C1 adsorption on A-TiO<sub>2</sub> (101) surface at 673 K can be calculate as equation below

$$\Delta G_{C1} = (-393.25) - (-387.50) - (-2.21) = -3.54 \text{ eV}$$

the results from the above in Table 7 was using to calculate the  $\Delta E_{ZPE}$  and  $\Delta G_{ads}$  are shown in Table C3.

**Table C3** The Gibbs free energy changes ( $\Delta G$ ) and ( $\Delta E_{ZPE}$ ) of carbon adsorption on A-TiO<sub>2</sub> (101) surface at 673 K

Carbon adsorption	$\Delta E_{ZPE}$ (eV)	$\Delta G_{ads}$ (eV)
C1	-4.37	-3.54
C2	-4.23	-3.34
C3	-2.57	-1.74

## REFERENCES

1. Al-Shafei, M.A., et al., *Deactivation Mechanism of Titania Catalyst*. Journal of Materials Science Research, 2016. **5**(4).
2. Argyle, M. and C. Bartholomew, *Heterogeneous Catalyst Deactivation and Regeneration: A Review*. Catalysts, 2015. **5**(1): p. 145-269.
3. Védrine, J., *Heterogeneous Catalysis on Metal Oxides*. Catalysts, 2017. **7**(11).
4. Carlucci, C., L. Degennaro, and R. Luisi, *Titanium Dioxide as a Catalyst in Biodiesel Production*. Catalysts, 2019. **9**(1).
5. M R Ranade 1, A.N., H Z Zhang, J F Banfield, S H Elder, A Zaban, P H Borse, S K Kulkarni, G S Doran, H J Whitfield. *Energetics of nanocrystalline TiO<sub>2</sub>*. 2002.
6. Li, J.-G. and T. Ishigaki, *Brookite→rutile phase transformation of TiO<sub>2</sub> studied with monodispersed particles*. Acta Materialia, 2004. **52**(17): p. 5143-5150.
7. Oi, L.E., et al., *Catalytic deoxygenation of triolein to green fuel over mesoporous TiO<sub>2</sub> aided by in situ hydrogen production*. International Journal of Hydrogen Energy, 2020. **45**(20): p. 11605-11614.
8. Li, C.-F., et al., *Defective TiO<sub>2</sub> for Propane Dehydrogenation*. Industrial & Engineering Chemistry Research, 2020. **59**(10): p. 4377-4387.
9. German, E., R. Faccio, and A.W. Mombrú, *A DFT +U study on structural, electronic, vibrational and thermodynamic properties of TiO<sub>2</sub> polymorphs and hydrogen titanate: tuning the Hubbard 'U-term'*. Journal of Physics Communications, 2017. **1**(5).
10. Perdew, J.P., K. Burke, and M. Ernzerhof, *Generalized gradient approximation made simple*. Physical Review Letters, 1996. **77**(18): p. 3865-3868.
11. Morgan, B.J. and G.W. Watson, *A DFT+U description of oxygen vacancies at the TiO<sub>2</sub> rutile (110) surface*. Surface Science, 2007. **601**(21): p. 5034-5041.
12. Grimme, S., et al., *A consistent and accurate ab initio parametrization of density functional dispersion correction (DFT-D) for the 94 elements H-Pu*. J Chem Phys, 2010. **132**(15): p. 154104.
13. Ortega, Y., et al., *A DFT study of the stoichiometric and reduced anatase (001)*

- surfaces. Applied Surface Science, 2014. **294**: p. 42-48.
14. Gharaei, S.K., M. Abbasnejad, and R. Maezono, *Bandgap reduction of photocatalytic TiO<sub>2</sub> nanotube by Cu doping*. Sci Rep, 2018. **8**(1): p. 14192.
  15. Arroyo-de Dompablo, M.E., A. Morales-Garcia, and M. Taravillo, *DFT+U calculations of crystal lattice, electronic structure, and phase stability under pressure of TiO<sub>2</sub> polymorphs*. J Chem Phys, 2011. **135**(5): p. 054503.
  16. Portillo-Vélez, N.S., et al., *Localized electronic states induced by oxygen vacancies on anatase TiO<sub>2</sub> (101) surface*. Surface Science, 2013. **616**: p. 115-119.
  17. Calzado, C.J., N.C. Hernández, and J.F. Sanz, *Effect of on-site Coulomb repulsion term on the band-gap states of the reduced rutile (110)TiO<sub>2</sub> surface*. Physical Review B, 2008. **77**(4).
  18. Rtetts, D.K.a.V.D.M., *Quantisierung als Eigenwertproblem*. 1926: p. 361-376.
  19. Kitchin, J., *Modeling materials using density functional theory*. Vol. 67. 2012, Cambridge Univ. Press. 1-298.
  20. Cococcioni, M., *The LDA+U Approach: A Simple Hubbard Correction for Correlated Ground States*, in *LDA+U for correlated materials*. 2012. p. 4.1-4.40.
  21. Himmetoglu, B., et al., *Hubbard-corrected DFT energy functionals: The LDA+U description of correlated systems*. International Journal of Quantum Chemistry, 2014. **114**(1): p. 14-49.
  22. Botton, S.D.a.G., *Electron-energy-loss spectra and the structural stability of nickel oxide an LSDA+U study*. PHYSICAL REVIEW B- Condens. Matter Mater. Phys., 1998. **57**: p. 1505-1509.
  23. Olinto da Silva, G. and J.B.L. Martins, *Effect of Hubbard parameter and semi-empirical van der Waals correction on benzene adsorption over anatase TiO<sub>2</sub> (1 0 1) surface*. Computational and Theoretical Chemistry, 2019. **1164**.
  24. Haus, J.W., *Nanophotonic devices*, in *Fundamentals and Applications of Nanophotonics*. 2016. p. 341-395.
  25. Lee, J.G., *Computational Materials Science An Introduction Second Edition*. 2017.

26. Salvato-Vallverdu, G., *periodic-boundaries-conditions*. 2009.
27. Cai, J., et al., *Nanostructured TiO<sub>2</sub> for light-driven CO<sub>2</sub> conversion into solar fuels*. APL Materials, 2020. **8**(4).
28. M. S, A., et al., *A Contemporary Assessment on Composite Titania onto Graphitic Carbon Nitride-Based Catalyst as Photocatalyst*. Journal of Energy and Safety Technology (JEST), 2019. **2**(1).
29. Lievens, C., et al., *A study of slow pyrolysis of one low rank coal via pyrolysis-GC/MS*. Fuel Processing Technology, 2013. **116**: p. 85-93.
30. Sonibare, O.O., T. Haeger, and S.F. Foley, *Structural characterization of Nigerian coals by X-ray diffraction, Raman and FTIR spectroscopy*. Energy, 2010. **35**(12): p. 5347-5353.
31. Bartholomew, C.H., *Mechanisms of catalyst deactivation*. Applied Catalysis A, 2001. **212**: p. 17-60.
32. Pan, X., et al., *Defective TiO<sub>2</sub> with oxygen vacancies: synthesis, properties and photocatalytic applications*. Nanoscale, 2013. **5**(9): p. 3601-14.
33. K. Kawamura, N.S., T. Inoue, T. Okumura, Y. Shimazu, and T. Okumura,, *Photoluminescence study of trap-state defect on TiO<sub>2</sub> thin film*. Journal of Physics: Conference Series, 2018. **995**.
34. Zhao, H., F. Pan, and Y. Li, *A review on the effects of TiO<sub>2</sub> surface point defects on CO<sub>2</sub> photoreduction with H<sub>2</sub>O*. Journal of Materiomics, 2017. **3**(1): p. 17-32.
35. I. Nakamura, N.N., S. Kutsuna, T. Ihara, S. Sugihara, and K. Takeuchi, *Role of oxygen vacancy in the plasma-treated TiO<sub>2</sub> photocatalyst with visible light activity for NO removal*. Journal of Molecular Catalysis A: Chemical, 2000. **161**(1-2): p. 205-212.
36. Gerosa, M., et al., *Defect calculations in semiconductors through a dielectric-dependent hybrid DFT functional: The case of oxygen vacancies in metal oxides*. J Chem Phys, 2015. **143**(13): p. 134702.
37. Hanaor, D.A.H. and C.C. Sorrell, *Review of the anatase to rutile phase transformation*. Journal of Materials Science, 2010. **46**(4): p. 855-874.
38. Hsiang, H.-I. and S.-C. Lin, *Effects of aging on the phase transformation and sintering properties of TiO<sub>2</sub> gels*. Materials Science and Engineering: A, 2004.

- 380(1-2): p. 67-72.
39. Frédéric Labat, P.B., and Carlo Adamo, *Structural and Electronic Properties of Selected Rutile and Anatase TiO<sub>2</sub> Surfaces: An ab Initio Investigation*. Journal of Chemical Theory and Computation, 2008. **4**(2): p. 341-352.
  40. Watson\*, B.J.M.a.G.W., *A Density Functional Theory + U Study of Oxygen Vacancy Formation at the (110), (100),(101),(001) Surface of Rutile TiO<sub>2</sub>*. J. Phys. Chem. C, 2009. **113**: p. 7322-7328.
  41. Samat, M.H., et al., *Hubbard U calculations on optical properties of 3 d transition metal oxide TiO<sub>2</sub>*. Results in Physics, 2016. **6**: p. 891-896.
  42. Araujo-Lopez, E., et al., *TiO<sub>2</sub> anatase's bulk and (001) surface, structural and electronic properties: A DFT study on the importance of Hubbard and van der Waals contributions*. Surface Science, 2016. **653**: p. 187-196.
  43. Cheng, H. and A. Selloni, *Surface and subsurface oxygen vacancies in anatase TiO<sub>2</sub> and differences with rutile*. Physical Review B, 2009. **79**(9).
  44. Kim, J., et al., *Plasma-Assisted Catalytic Effects of TiO<sub>2</sub> /Macroporous SiO<sub>2</sub> on the Synthesis of Light Hydrocarbons from Methane*. ChemCatChem, 2020. **12**(20): p. 5067-5075.
  45. Paunović, V., et al., *Activity differences of rutile and anatase TiO<sub>2</sub> polymorphs in catalytic HBr oxidation*. Catalysis Today, 2020.
  46. Praserttham, S., et al., *Performance controlled via surface oxygen-vacancy in Ti-based oxide catalyst during methyl oleate epoxidation*. Sci Rep, 2020. **10**(1): p. 18952.
  47. Zhu, L., Q.M. Hu, and R. Yang, *The effect of electron localization on the electronic structure and migration barrier of oxygen vacancies in rutile*. J Phys Condens Matter, 2014. **26**(5): p. 055602.
  48. Vu, N.H., et al., *Anatase-rutile phase transformation of titanium dioxide bulk material: a DFT + U approach*. J Phys Condens Matter, 2012. **24**(40): p. 405501.
  49. Tolba, S.A., et al., *The DFT+U: Approaches, Accuracy, and Applications, in Density Functional Calculations - Recent Progresses of Theory and Application*.

- 2018.
50. Abbasi, A. and J.J. Sardroodi, *A van der WAALS CORRECTED DFT STUDY OF CHEMICAL SENSING OF SULFUR DIOXIDE MOLECULE BY NITROGEN-DOPED Au DECORATED TiO<sub>2</sub> NANOPARTICLES*. *Surface Review and Letters*, 2018. **25**(06).
  51. Mohamad, M., et al., *A density functional study of structural, electronic and optical properties of titanium dioxide: Characterization of rutile, anatase and brookite polymorphs*. *Materials Science in Semiconductor Processing*, 2015. **31**: p. 405-414.
  52. Sorescu, D.C., et al., *CO<sub>2</sub> adsorption on TiO<sub>2</sub>(110) rutile: insight from dispersion-corrected density functional theory calculations and scanning tunneling microscopy experiments*. *J Chem Phys*, 2011. **134**(10): p. 104707.
  53. Elahifard, M., et al., *Dispersion of Defects in TiO<sub>2</sub> Semiconductor: Oxygen Vacancies in the Bulk and Surface of Rutile and Anatase*. *Catalysts*, 2020. **10**(4).
  54. Yang, F., et al., *Prediction of Structural and Electronic Properties of C and Cl<sub>2</sub> Adsorbed on the Rutile TiO<sub>2</sub> (110) Surface*. *ACS Omega*, 2020. **5**(45): p. 29002-29008.
  55. L. Kavan, M.G., S. E. Gilbert, C. Klemenz, and H. J. Scheel, *Electrochemical and Photoelectrochemical Investigation of Single-Crystal Anatase*. *Journal of the American Chemical Society*, 1996. **118**: p. 6716-6723.
  56. Burdett, J.K., et al., *Structural-electronic relationships in inorganic solids: powder neutron diffraction studies of the rutile and anatase polymorphs of titanium dioxide at 15 and 295 K*. *Journal of the American Chemical Society*, 1987. **109**(12): p. 3639-3646.
  57. Zhang, L., et al., *Facile fabrication and characterization of multi-type carbon-doped TiO<sub>2</sub> for visible light-activated photocatalytic mineralization of gaseous toluene*. *Journal of Materials Chemistry A*, 2013. **1**(14).



จุฬาลงกรณ์มหาวิทยาลัย  
**CHULALONGKORN UNIVERSITY**

**VITA**

<b>NAME</b>	Chinanag Ngamlaor
<b>DATE OF BIRTH</b>	27 June 1997
<b>PLACE OF BIRTH</b>	Rayong
<b>HOME ADDRESS</b>	No. 6 Soi.Maptaphut 3, Wat Maptaphut Road, Maptaphut Sub-district, Muang Rayong District, Rayong, 21150





จุฬาลงกรณ์มหาวิทยาลัย  
**CHULALONGKORN UNIVERSITY**